Elasticity of Materials at High Pressure

By

Arianna Elizabeth Gleason

A dissertation submitted in partial satisfaction of the
Requirements for the degree of
Doctor of Philosophy

in

Earth and Planetary Science

in the

GRADUATE DIVISION
of the
UNIVERSITY OF CALIFORNIA, BERKELEY

Committee in charge:
Professor Raymond Jeanloz, Chair
Professor Hans-Rudolf Wenk
Professor Kenneth Raymond

Fall 2010

Elasticity of Materials at High Pressure

Abstract

Elasticity of Materials at High Pressure
by
Arianna Elizabeth Gleason
Doctor of Philosophy in Earth and Planetary Science
University of California, Berkeley
Professor Raymond Jeanloz, Chair

The high-pressure behavior of the elastic properties of materials is important for condensed matter and materials physics, and planetary and geosciences, as it contributes to the mechanical deformations and stability of solids under external stresses. The high-pressure elasticity of relevant minerals is of substantial geophysical importance for the Earth's interior since they relate to (1) velocities of seismic waves and (2) the change in density that occurs when minerals are under pressure. Absence of samples from the deep interior prompts comparisons between seismological observations and the elastic properties of candidate minerals as a way to extract information regarding the composition and mineralogy of the Earth.

Implementing a new method for measuring compressional- and shear-wave velocities, V_p and V_s, based on Brillouin spectroscopy of polycrystalline materials at high pressures, I examine four case studies: 1) soda-lime glass, 2) NaCl, 3) MgO, and 4) Kilauea basalt glass. The results on multigrain soda-lime glass show that even with an index differing by 3 percent, an oil medium removes the effects of multiple scattering from the Brillouin spectra of the glass powders; similarly, high-pressure Brillouin spectra from transparent polycrystalline samples should, in many cases, be free from optical-scattering effects. I measure seismic wave velocities of polycrystalline NaCl (halite) to 30.5 GPa at room temperature, finding the bulk and shear moduli and pressure derivatives to be: $K_T = 23.75$ (± 0.08) GPa, $K_T' = 5.32$ (±0.1), $G = 14.9$ (± 0.5) GPa, $G' = 2.6$ (± 0.5). The resulting equation of state agrees well with previous x-ray diffraction measurements, illustrating the suitability of high pressure Brillouin scattering to characterize the elasticity of polycrystalline materials. Brillouin scattering of non-hydrostatically compressed and decompressed polycrystalline MgO (periclase) to 60 GPa documents shear- and compressional-wave velocities ~20% lower than the Voigt-Reuss-Hill average values calculated from measurements on hydrostatically compressed single crystals. Calculations on the effects of non-hydrostaticity reveal that the sound wave velocities can be lowered, however, the calculated magnitude cannot explain our observations. I discuss possible additional causes for these anomalously low velocity trends, including grain size, grain boundary effects, preferred orientation, and impurities. High pressure Brillouin spectroscopy of natural Kilauea basalt glass not only provides measurements of elastic moduli and density, but I also find a reversible structure change over 0 - 22 GPa. As glass at high pressure is used as a proxy for melt or magma at high pressure, this ultimately documents a structural change in the magma and has implications for the buoyancy of silicate melts in terrestrial planets.

Professor Raymond Jeanloz
Dissertation Committee Chair

Contents

List of Figures ii
Symbols and Abbreviations iv
1 Introduction 1
Bibliography 3
2 Grain-boundary effects in Brillouin scattering at ambient and high pressure 4
Bibliography 9
3 Elasticity and refractive index of NaCl at high pressure 10
Bibliography 17
4 Low sound velocities in polycrystalline MgO under non-hydrostatic compression 19
Bibliography 27
5 Structural stability and sound velocity of Kilauea basalt glass 30
Bibliography 36
A Derivations 38
Bibliography 41

List of Figures

2.1 Brillouin scattering geometries 5
2.2 Soda-lime glass Brillouin spectra at ambient conditions 6
2.3 Soda-lime glass Brillouin spectra at high pressure 8

3.1 NaCl compressional and shear velocities as a function of pressure 12
3.2 (a) Rotational dependence of NaCl at P = 0.75 GPa 13
(b) Spatial variation of NaCl 13
3.3 Compressional mode frequency shifts Refractive index as a function of pressure for NaCl 14
3.4 Density as a function of pressure for NaCl 15
3.5 Shear modulus as a function of pressure for NaCl 16

4.1 Compressional and shear velocities as a function of pressure for MgO 21
4.2 Brillouin scattering spectra of polycrystalline MgO 23
4.3 Maximum shear stress of polycrystalline MgO 24
4.4 Calculated MgO velocities under uniaxial compression 25

5.1 Compressional and shear velocities for Kilauea basalt glass 32
5.2 Compressional mode and refractive index as a function of pressure for Kilauea basalt glass 33
5.3 Elastic moduli and density as a function of pressure Kilauea basalt glass 34

Acknowledgements

Raymond Jeanloz ~ Thank you for having faith in me, especially in the beginning. Your confidence in me made this possible; from the bottom of my heart, thank you.

Bonnie June Low Gleason ~ You will never read this, but you are always next to me, hand in hand, every step of the way. Your strength is my inspiration. I miss you everyday.

Robert Charles Gleason ~ We played together to the horses on this one pop, all my love.

Howard Stringer Gleason ~ This is for you … and all the hardworking Gleason's in our past.

Hesper Elizabeth Gleason ~ Your energy inspires me everyday, thank you for your constant sparkle.

Della Anne Gleason ~ You are always my **happiest** thought, everyday of my life.

Spencer Greg Hoyt Gleason ~ Thank you for all your kind words, kind ways and unwavering brotherly love.

Bryan Keith Holbrook ~ Amazing strength, love, companionship and unwavering support for which I am indebted and truly grateful.

Brent M. Grocholski, Ryan S. McWilliams, Dylan K. Spaulding & Zack M. Geballe ~ My high pressure brothers ... how I have learned so much from you. I thank you for all your love, advice and support.

Nicole Schlegel, Suzanne J. Ali, Marius A. Millot & Laura Robin Benedetti ~ Outstanding officemates and wonderful friends, thank you for always looking out for me through thick and thin.

Harley & Rizzo ~ My good boys. I love you both, thank you for looking out for mamas.

Bin Chen ~ We make the best team. Thank you for a wonderful experience in science and for being a treasured friend.

Spacewatch Asteroid Survey, Dr. Robert McMillan & Dr. Jeffery Larsen ~ From the bottom of my heart, thank you for having faith in me in the very very beginning.

Symbols

Variables

P	Pressure (GPa)
V	Volume (cm^3)
V_p	Compressional or longitudinal wave speed (km/s)
V_s	Shear or transverse wave speed (km/s)
K	Bulk modulus (GPa)
K'	Pressure derivative of bulk modulus
K''	2nd pressure derivative of bulk modulus (GPa^{-1})
G	Shear modulus (GPa)
G'	Pressure derivative of shear modulus
ρ	Density (g/cm^3)
n	Refractive index
θ	Scattering angle (^{o})
λ	Wavelength (nm)
$_S$	Adiabatic
$_T$	Isothermal
d	d-spacing (Å)
ω	Frequency shift (GHz)
$_{180}$	Measured in backscatter geometry
$_{70}$	Measured in equal-angle geometry
C_v	Isochoric specific heat (Jmol^{-1}K^{-1})
α	Thermal expansivity (K^{-1})
γ	Grüneisen parameter
c_{ij}	Single-crystal elastic moduli (GPa)
C_p	Isobaric specific heat (Jmol^{-1}K^{-1})
$[hkl]$	Direction in a crystal
$\sigma_{[hkl]}$	Uniaxial stress (GPa)
f	Eulerian finite strain metric
F	Normalized stress (GPa)
ϕ	Helmholtz's potential
m	Mass (kg)

Chapter 1

Introduction

Elastic properties govern the behavior of a material subjected to small stresses, such as those associated with seismic waves. The relationship between stress and strain (deformation) in the region of elastic behavior is the elastic modulus. The bulk modulus describes how much pressure is required to cause a unit volume change; whereas the shear modulus, or rigidity, involves no volume change, but describes a material's change in shape as a response to shear stresses. Elasticity measurements provide information concerning the forces that operate between atoms or ions, giving insight into the nature of binding forces in crystals.

Elastic constants dictate the propagation of sound (elastic) waves in a medium, including the elastic anisotropy of the material [*Birch*, 1952]. Elastic properties can be determined from the measurement of acoustic wave propagation in a material by identifying the forces as functions of stress (via application of Hooke's Law) with the associated strain components as a displacement (mechanical) wave that propagates through the material [*Mason*, 1958]. Dynamic equilibrium (conservation of linear momentum) ensures that these forces are equal to inertial forces, which show how the displacements vary with time according to Newton's second law as described by a set of wave equations [*Love*, 1944]. For example, in a cubic material, symmetry reduces the number of independent elastic constants, and solutions result in one compressional wave and two shear waves [*Schreiber et al.,* 1973].

Accurate experimental constraints on the Earth and planetary interiors require knowledge of a great variety of physical and chemical properties of minerals obtained under pertinent pressure-temperature conditions. To measure the elasticity of Earth-relevant minerals, the most direct and oldest method involves exerting a sustained pressure on a sample (static compression) and measuring the volume change. Experimentally, this can be achieved using x-ray diffraction to monitor the change in distance between atomic lattice planes (d-spacing) using Bragg's Law ($\lambda = 2d \sin\theta$: λ and θ are wavelength and scattering angle, respectively) with increasing pressure. By measuring several d-spacings at each pressure P, the atomic unit-cell volume is known [*Stout and Jensen*, 1989]. The bulk modulus $K = -V(dP/dV) = \rho(dP/d\rho)$ can be obtained in this way, but the shear modulus cannot be measured using P–V data ($\rho = m/V$ is density). A more powerful method would include the measurement of shear *and* compressional wave speeds at high pressure: this would determine both bulk and shear moduli, and ultimately quantify second- and higher-order derivatives of the inter-atomic potential with strain. Brillouin spectroscopy is a light scattering technique that allows one to measure the acoustic wave speeds of a material.

Brillouin spectroscopy involves measuring the inelastic scattering of light by sound waves, or thermal excitations, in a material [*Dil*, 1982]. Some of the incident light is Doppler shifted by scattering from acoustic phonons in a material; measuring this shift, and applying conservation of energy and momentum, one can determine the sound velocity. Combining this technique with a device to generate high pressure, the diamond-anvil cell, we have a powerful method for monitoring the elasticity of geologically important materials at elevated pressure-temperature conditions [e.g., *Weidner et al*., 1975; *Duffy et al.,* 1995; *Murakami et al.,* 2007].

The study of elasticity of Earth materials has become increasingly important over the past decade, as contributions from global seismic tomography, seismological investigations of geographically and radially localized regions, mantle discontinuities, and analysis of normal modes of oscillations have revealed the Earth's mantle in unprecedented detail [e.g., *Ishii and Tromp*, 1999]. To the extent that the interior of the Earth behaves elastically, the propagation of seismic waves is determined by the elastic constants of the component materials. Here I present measurements using Brillouin spectroscopy to determine acoustic velocities of a number of different multi-grain or polycrystalline materials at ambient and high pressure. The first part of this thesis will address the reliability of polycrystalline Brillouin spectroscopy at high pressure by characterizing multigrain soda-lime glass and polycrystalline NaCl; the second part will apply this technique to more geophysically relevant materials, MgO (periclase) and a natural Kilauea basalt glass.

Bibliography

Birch, F. (1952), Elasticity and constitution of the Earth's interior, *J. Geophys. Res. 57*, 227 – 286.

Dil, J.G. (1982), Brillouin scattering in condensed matter, *Rep. Prog. Phys., 45*, 285 – 334.

Duffy, T., et al. (1995), Elasticity of forsterite to 16 GPa and the composition of the upper mantle, *Nature, 378*, 170 – 173.

Ishii, M., and J. Tromp (1999), Normal-mode and free-air gravity constraints on lateral variations in velocity and density of the Earth's mantle, *Science, 285*, 1231 – 1236.

Mason, W. (1958), Physical acoustics and the properties of solids, D. Van Nostrand Company, Inc., pp. 368 – 380, Princeton, New Jersey.

Murakami, M., et al. (2007), Sound velocity of $MgSiO_3$ post-perovskite phase: A constraint on the D" discontinuity, *Earth and Planet. Sci. Lett., 259*, 18 – 23.

Love, A. (1944), A treatise on the mathematical theory of elasticity, Dover publications, pp. 297 – 302, New York.

Schreiber, E., et al. (1973), Elastic constants and their measurements, McGraw-Hill Book Company, New York.

Stout, G.H., and L. Jensen (1989), X-ray structure determination, A practical guide, John Wiley and Sons, Inc., New York.

Weidner, D., et al. (1975), Elasticity of microcrystals, *Geophys. Res. Lett., 2*, 189 – 192.

Chapter 2

Grain-boundary effects in Brillouin scattering at ambient and high pressure

Although refraction of light at grain boundaries can significantly alter Brillouin spectra – hence inferred acoustic velocities – of powder samples, we demonstrate that the effects of (multiple) elastic scattering can be eliminated through 1) use of refractive index-matching oils or 2) application of high pressures (≥ 1 GPa). In this manner, we determine the acoustic-wave velocities of soda-lime glass powder to pressures of 13 GPa, finding good agreement with previous measurements on bulk samples. Our results provide a baseline for reliable acoustic-wave velocity measurements at high pressures via Brillouin spectroscopy on polycrystalline samples.

Brillouin spectroscopy is a well-established technique for determining the acoustic-wave velocities of single crystals under pressure [e.g., *Bassett and Brody*, 1977]. Such laboratory measurements are crucial for interpreting seismological observations of Earth's interior, including the rich data provided by seismic tomography [e.g., *Su and Dziewonski*, 1997], yet they are limited by phase transitions, shear stresses and heating, all of which compromise the integrity of single-crystal samples. More generally, it may be impossible to maintain a given sample material in single-crystal form, which motivates establishing methods for obtaining elastic moduli from powders.

Hernandez et al. [1996] showed that Brillouin spectra of powders differ significantly from those of the corresponding bulk (transparent) materials, and proposed that this difference can be attributed to multiple elastic scattering at grain boundaries (grain-air interfaces). They documented quantitative agreement between their elastic-scattering model and Brillouin spectra collected from bulk and powder samples. Here we confirm their results through additional measurements, in which we modify the grain-boundary scattering by way of an index-matching medium [e.g., *Weidner et al.,* 1975] or by application of quasi-hydrostatic pressure, and collect Brillouin spectra in several different geometries [e.g., *Zha et al.,* 1994]. We use silicate glass samples in order to eliminate the effects of acoustic or optical birefringence, the directional dependencies that, in general, characterize the velocities of sound and light in crystals.

Brillouin spectra were collected using 0.25-0.50 W of polarized 532 nm radiation from a continuous-wave Nd:YVO_4 laser, along with a scanning Sandercock six-pass tandem Fabry-Perot interferometer in a confocal geometry adapted from the angle-dispersive system described by *Koski and Yarger* [2005]. The laser-beam diameter is ~25 μm at the sample. Spectra are obtained in back-scatter, reflection or transmission geometry, with a scattering angle θ (Figure

2.1); no analyzer is used. For back-scatter geometry (Figure 2.1a), the wave velocity (V) is given by:

$$V = \frac{(\omega)\lambda_0}{2n\sin\left(\frac{\theta}{2}\right)} \tag{2.1}$$

and similarly for reflection geometry (Figure 2.1b):

$$V = \frac{(\omega)\lambda_0}{2\sqrt{n^2 - \cos^2\left(\frac{\theta}{2}\right)}} \tag{2.2}$$

where ω is the measured Brillouin frequency shift, λ_0 is the incident laser wavelength and n is the refractive index of the sample. For equal-angle transmission with a parallel-sided platelet sample (Figure 2.1c), the refractive index drops out of (2.1) [*Whitfield et al.,* 1976]. Because of the effects of multiple elastic scattering, it is often easiest to collect Brillouin spectra from powders using back-scatter geometry and most difficult using transmission geometry. However, only the compressional (longitudinal) mode appears in spectra collected in back-scatter geometry, whereas both compressional and shear (transverse) modes can appear in transmission and reflection spectra, albeit with reduced intensity in the latter case.

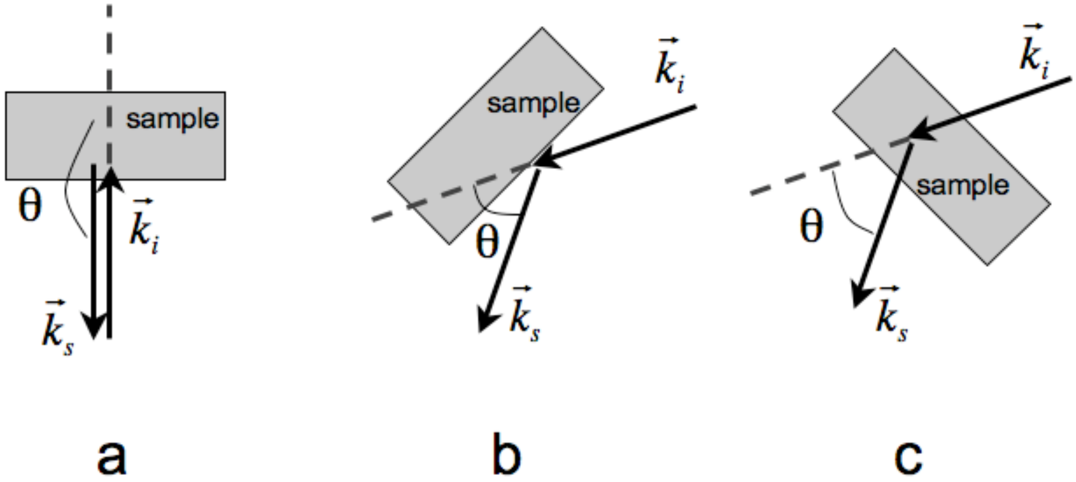

Figure 2.1: Brillouin scattering geometries used in the present study include (**a**) back-scatter (θ = 180˚), (**b**) reflection (θ = 70˚) and (**c**) transmission (θ = 70˚), with θ being the scattering angle defined such that for wavevectors describing the incident ($\mathbf{k_i}$) and Brillouin-scattered ($\mathbf{k_s}$) light, $\mathbf{k_s} - \mathbf{k_i} = 2\,\mathbf{k_i}\sin(\theta/2)$ [*Dil*, 1982].

Brillouin spectra were collected at room temperature and pressure from both bulk and powder (6 μm average grain size) forms of Erie Electroverre soda-lime glass (index of refraction n = 1.517 at a wavelength of 546.1 nm), having a density of 2.48 g/cc and a composition of: 72.20% SiO_2; 14.30% NaO; 6.40% CaO; 4.30% MgO; 1.20% Al_2O_3; 1.20% KO; 0.03% SO_3; 0.03% FeO [D. Bertwell, Erie Electroverre, *personal communication*, 2009]. Spectra were also collected from multi-grain samples at high pressure, using a gasketted diamond-anvil cell with a 4:1 methanol:ethanol pressure-transmitting medium and ruby fluorescence to calibrate the pressure [e.g., *Bassett and Brody*, 1977].

In our study, each spectrum is folded about the central Rayleigh peak in order to enhance the Brillouin signal from the sample. We do this by first removing the Rayleigh peaks, folding the Stokes onto the anti-Stokes component of the spectrum, and determining optimal alignment between the two components by maximizing their cross-correlation (calculated as a function of lag in integer units of the detector resolution, 0.05725 GHz). Once aligned, the folded Stokes and anti-Stokes components of the spectrum are averaged, and we do not retain any amplitude difference between the two.

Brillouin spectra from dry powders (Figure 2.2, *bottom* two traces) show the characteristic asymmetry documented by *Hernandez et al.* [1996]: intensity increases faster than linearly with increasing frequency shift (proportional to velocity) up to a maximum, corresponding to $\theta = 180^\circ$ regardless of scattering geometry, and then falls rapidly to the background shown by horizontal dashed lines. *Hernandez et al.*'s [1996] multiple elastic-scattering model (their equation (16), shown by solid grey lines in the lower two traces of Figure 2.2) provides a good fit to our data, and the acoustic velocity is then given by the maximum of the asymmetric peak.

If this model is correct, it should be possible to eliminate the effects of multiple scattering by immersing the powder sample in a medium that matches the index of refraction of the glass, a practice long employed by optical mineralogists (i.e. Becke line test). We find that this is the case, and recover the expected (nearly) symmetric peaks of the bulk sample by using glycerin oil as an index-matching medium (Figure 2.2, *top* traces); the oil has an index of refraction n = 1.473 [*Weast*, 1979].

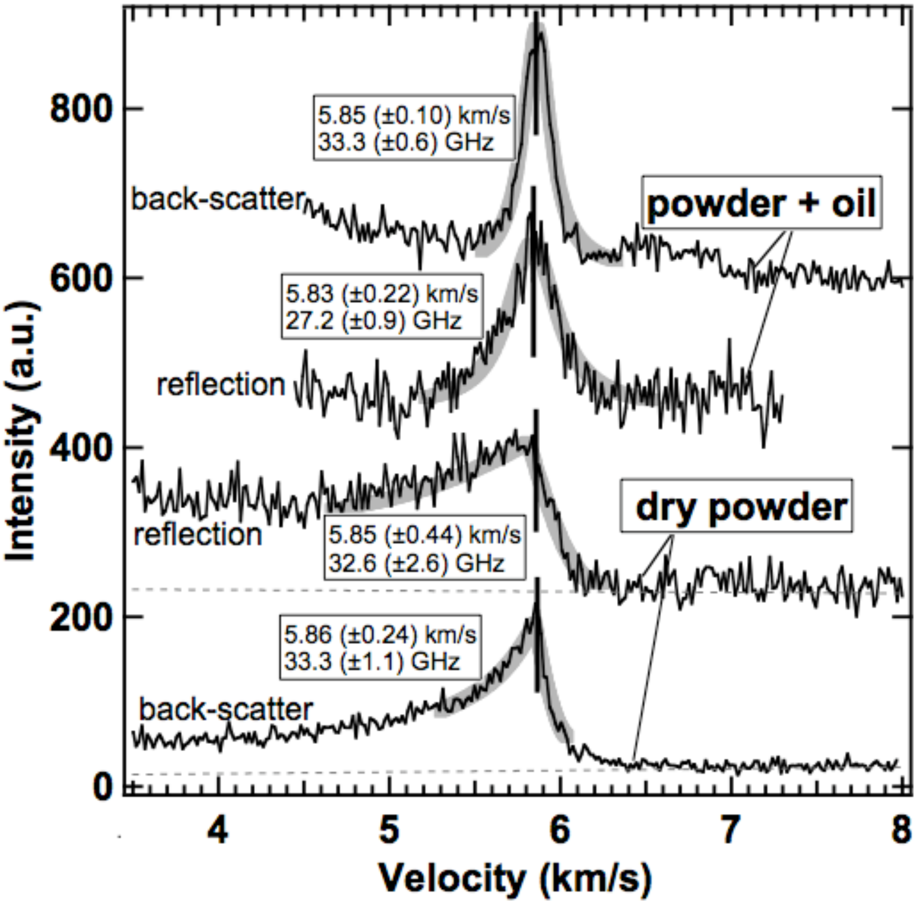

Figure 2.2: Brillouin spectra (*black* traces) of soda-lime glass powder at ambient conditions (P = 0 GPa, T = 290 K) in back-scatter (*top* and *bottom* spectra: $\theta = 180^\circ$) and reflection geometries (*middle* two spectra: $\theta = 70^\circ$), plotted as a function of velocity rather than frequency shift in order to document alignment of the acoustic peaks. The *bottom* two traces are from dry powder and the *top* two traces from powder in an index-matching oil. Fits to the peaks are shown by solid grey lines, with the peak locations indicated by vertical lines (values for frequency shifts and corresponding velocities, along with their uncertainties, are given in the boxes).

Gaussian fits to these peaks yield acoustic velocities indistinguishable from those derived from the bulk glass (Figure 2.3): V_P = 5.9 km/s (uncertainties quoted in the figures correspond to ± half-width at half-maximum, and provide conservative estimates of the best-fit values for the velocities). Note, however, that the measured frequency shifts depend on scattering angle, as expected from (2.1). Because they correspond to a single scattering angle θ in each case, the Brillouin peaks from the powder immersed in oil and from the bulk glass are both narrower than for dry powders.

These results further confirm *Hernandez et al.*'s [1996] model, and provide new experimental strategies for mitigating the effects of multiple-elastic scattering in Brillouin spectra of powder (including polycrystalline) samples. Rather than immersing the powder in an index-matching medium, sintering offers another means of reducing multiple-scattering in the Brillouin spectra of multi-grain samples [e.g., *Sinogeikin et al.*, 2004; *Murakami et al.*, 2007]. This can be accomplished through application of quasi-hydrostatic pressures, even at room temperature, as illustrated in Figure 2.3 (see also *Ahart et al.* [2006]).

We find that our high-pressure powder spectra are characterized by symmetric peaks, as is the case for the bulk sample or the powders immersed in an index-matching medium at zero pressure (Figures 2.2, 2.3). The spectra are qualitatively different from those affected by multiple-elastic scattering, in this regard, and yield results in quantitative agreement with independent measurements of room-temperature acoustic-wave velocities as a function of pressure. Our value V_P = 8.0 (± 0.1) km/s at 13 GPa, for example, is in good agreement with *Grimsditch et al.*'s [1984] and *Xu*'s [1996] experiments on silica glass, as well as with the ultrasonic and Brillouin measurements of *Li et al.* [2000] and *Tkachev et al.* [2005] on soda-lime glass (Figure 2.3). As with the zero-pressure spectra, the peaks are observed at different frequency shifts, depending on scattering angle θ, yet the resulting acoustic-wave velocities are entirely consistent with each other.

Evidently the grain boundaries effectively disappear under the influence of pressure, with neighboring grains providing an (approximately) index-matching medium for each other, as expected from porosity reduction. This finding is applicable to polycrystalline samples, not just glass powders, because the indices of refraction of crystals often show only small variation as a function of direction. That is, the birefringence – the maximum difference in index of refraction as a function of orientation – is less than ± 3-5 percent for many minerals, albeit with some notable exceptions [*Weast*, 1979]. We found that even with an index differing by 3 percent, the oil medium removes the effects of multiple scattering from the Brillouin spectra of our glass powders (Figure 2.2). Therefore, high-pressure Brillouin spectra from transparent polycrystalline samples should in many cases be free from optical-scattering effects, and the results would then reflect the geophysically relevant (and orientation-dependent) acoustic wave velocities of the corresponding bulk sample.

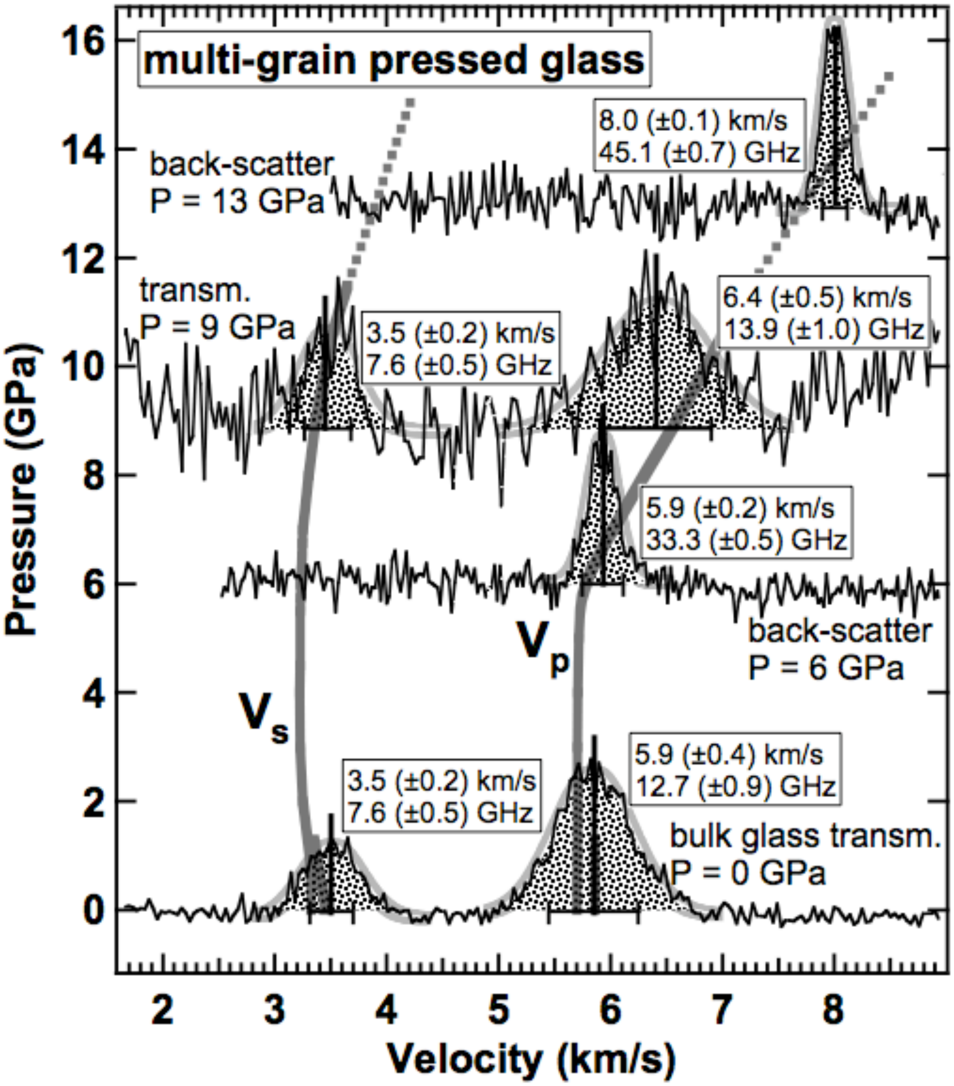

Figure 2.3: Brillouin spectra (*black* traces) of bulk glass at zero pressure (*bottom*: transmission geometry), and of pressed glass powder (*upper* three traces) at 6, 9 and 13 GPa (transmission and back-scatter geometries, with only the compressional mode visible in back-scattering). The traces are shifted so as to match the baseline for each spectrum with the pressure scale (*left*). Gaussian fits are shown as *solid grey* curves, with *vertical lines* indicating peak positions (velocities and frequency shifts, along with uncertainties, given in the boxes); horizontal error bars on peak locations are lined up with the baseline for the corresponding spectrum. The refractive index of the glass, required to calculate velocities from back-scatter measurements (see (2.1)), is determined as a function of pressure from the combination of transmission and reflection/back-scatter data. *Thick solid grey* curves show compressional (V_P) and shear (V_S) wave velocities for float glass as a function of pressure, based on *Li et al.*'s [2000] ultrasonic measurements to 1.3 GPa and on *Tkachev et al.*'s [2005] Brillouin measurements to 12 GPa.

Bibliography

Ahart, M., et al. (2006), High-pressure Brillouin scattering of amorphous BeH_2, *J. Chem. Phys., 124*(1), 014502, doi:10.1063/1.2138692.

Bassett, W.A., and E. B. Brody (1977), Brillouin scattering: A new way to measure elastic moduli at high pressures, in *High-Pressure Research: Applications in Geophysics*, edited by M. H. Manghnani and S. Akimoto, pp. 503 – 508, Academic Press, New York.

Dil, J. G. (1982), Brillouin scattering in condensed matter, *Rep. Prog. Phys., 45*, 285 – 334.

Grimsditch, M. (1984), Polymorphism in amorphous SiO_2, *Phys. Rev. Lett., 52*(26), 2379 – 2381.

Hernandez, J., et al. (1996), Low-frequency light-scattering spectroscopy of powders, *J. Opt. Soc. Am. B, 13*(6), 1130 – 1134, doi:10.1364/JOSAB.13.001130.2

Koski, K.J., and J. L. Yarger (2005), Brillouin imaging, *Appl. Phys. Lett., 87*, 61903.

Li, F.-Y., et al. (2000), Elastic properties of float glass and SiO_2+TiO_2 glass under high pressure, *Acta Phys. Sin., 49*(11), 2129 – 2131, doi:10.1088/1000-3290/49(11)/2129-04.

Murakami, M., et al. (2007), Sound velocity of $MgSiO_3$ perovskite to Mbar pressure, *Earth Planet. Sci. Lett., 256*, 47 – 54, doi:10.1016/j.epsl.2007.01.011.

Sinogeikin, S. V., et al. (2004), Elasticity of single crystal and polycrystalline MgSiO3 perovskite by Brillouin spectroscopy, *Geophys. Res. Lett. 31*, L06620.

Su, W.-j., and A. M. Dziewonski (1997), Simultaneous inversion for 3-D variation in shear and bulk velocity in the mantle, *Phys. Earth Planet. Inter., 100*, 135 – 156, doi:10.1016/S0031-9201(96)03236-0.

Tkachev, S. N., et al. (2005), In situ Brillouin spectroscopy of a pressure-induced apparent second-order transition in silicate glass, *Phys. Rev. Lett., 95*, 057402, doi:10.1103/PhysPevLett.95.057402.

Weast, R. C. (Ed.) (1979), *CRC Handbook of Chemistry and Physics,* 59th ed., CRC Press Inc., Florida, ISBN 0-8439-0459-8.

Weidner, D. J., et al. (1975), Elasticity of Microcrystals, *Geophys. Res. Lett.,* 2, 189 - 192, doi:10.1029/GL002i005p00189.

Whitfield, C. H., et al. (1976), Elastic moduli of NaCl by Brillouin scattering at high pressure in a diamond anvil cell, *Rev. Sci. Instrum., 47*(8), 942 – 947, doi:10.1063/1.1134778.

Xu, J. (1996), Brillouin scattering and ultrasonic studies at high temperature and high pressure, *Chem. Geol., 128*, 17 – 24, doi:10.1016/0009-2541(95)00160-3.

Zha, C.-s., et al. (1994), Acoustic velocities and refractive index of SiO_2 glass to 57.5 GPa by Brillouin scattering, *Phys. Rev. B*, 50, 105 – 112, doi/10.1103/PhysRevB.50.13105

Chapter 3

Elasticity and refractive index of NaCl at high pressure

Brillouin spectroscopy of polycrystalline NaCl (halite), measured to peak pressures of 31 GPa at room temperature, documents isotropic elastic moduli in good agreement with previous single-crystal Brillouin: compressional velocity $V_p = 4.78$ *to* 8.63 *(± 0.01) km/s, shear velocity* $V_s = 2.70$ *to* 3.59 *(± 0.08) km/s and index of refraction* $n = 1.54 - 1.81$ *at 0.8 – 30.5 GPa. Eulerian finite-strain analysis yields the bulk modulus and pressure derivative* $K_T = 23.75$ *(± 0.08) GPa,* $K_T' = 5.32$ *(± 0.1) and* $K_T'' = -0.55$ *(± 0.1)* GPa^{-1} *at zero pressure. The results illustrate the suitability of high-pressure Brillouin scattering for characterizing the elasticity of polycrystalline materials.*

Brillouin spectroscopy is an important tool for determining the acoustic velocities and elastic moduli of solids [*Dil,* 1982], with measurements on single crystals being routinely used to characterize elasticity at high pressures [e.g., *Whitfield et al.,* 1976]. However, the high pressure-temperature conditions of Earth's mantle (up to 130 GPa, 2500 K) compromises the integrity of single-crystal samples, whether through phase transitions or strains caused by shear stresses and heating. Thus, Brillouin scattering has been reported to 81 GPa for single crystals [*Marquardt et al.,* 2009], whereas measurements on polycrystals have reached more than twice that pressure [*Murakami et al.,* 2007]. In addition, numerous mantle phases have not been synthesized as single-crystals of sufficient size for single-crystal Brillouin studies.

Previous studies have illustrated the suitability of polycrystalline Brillouin spectroscopy for extracting average acoustic-wave velocities [e.g., *Campbell and Heinz,* 1992; *Murakami et al.,* 2009, *Gleason et al.,* 2009; *Chen et al.,* 2010]. Here, we present Brillouin measurements on polycrystalline NaCl as a benchmark material, comparing the results with independent data from single-crystal Brillouin spectroscopy [*Whitfield et al.,* 1976], x-ray diffraction [*Sato-Sorensen*, 1983], ultrasonic measurements [*Spetzler et al.,* 1972; *Frankel et al.,* 1976] and shock-wave experiments [*Fritz et al.,* 1968]. NaCl is also of interest as a pressure-transmitting medium and calibrant [*Birch,* 1978; *Brown,* 1999].

NaCl powder (Mallinckrodt, 99.99% purity) was crushed to 2-5 μm grain size, as determined by visual inspection. Diamond-anvils (culet diameter of 300 μm) were used in a short symmetric cell (ungasketted) to press a transparent platelet of vacuum dried, ground NaCl to 40μm thickness. A spring-steel gasket – initially 250 μm thick, pre-indented to 45 μm – with a 100 μm hole served to contain the polycrystalline NaCl platelet plus 4 – 6 ruby spheres as pressure calibrants. For a given pressure, we collected Brillouin spectra at 4 - 8 locations across the sample and/or varied rotational orientations up to 330° (in 30° – 45° increments) about the incident laser beam axis. Collection times of 5 - 30 minutes were sufficient to give data with adequate counting statistics.

Using confocal optics and 0.25-0.5 W of polarized λ = 532 nm radiation from a continuous wave Nd:YVO_4 laser, spectra are obtained with a six-pass tandem (Sandercock) Fabry-Perot interferometer in either backscatter (θ = 180°) or equal-angle (θ = 70°) scattering geometry through a diamond-anvil cell. Measurements at two scattering angles (θ) allow us to determine the index of refraction (n) as well as the acoustic-wave velocities as a function of pressure from the sample inside the diamond-anvil cell [e.g., *Chen et al.,* 2010]. The laser beam, ~20 μm diameter in the sample, acts as the probe, and with a fluorescence spectrometer integrated into the Brillouin system, *in situ* pressure measurements are made without moving the sample. Data were collected on compression and decompression for both scattering geometries. Each spectrum is folded about the central Rayleigh peak in order to enhance the Brillouin signal from the sample [*Gleason et al.,* 2009], and peaks are fit with a Gaussian profile.

For equal-angle transmission through a parallel-sided platelet, the wave velocity (V) for shear ($_s$) or compressional ($_p$) modes is given by $V_{s,p} = \omega\lambda_0 / 2\sin\left(\theta/2\right)$, where ω and λ_0 are the measured frequency shift and incident laser wavelength, respectively. The wave velocities increase smoothly with pressure, V_p ranging from 4.78 to 8.63 (± 0.01) km/s at 0-30.5 GPa and V_s = 2.70 to 3.59 (± 0.08) km/s at 0-18.7 GPa, respectively (Figure 3.1). The shear mode becomes too weak to measure beyond 19 GPa on compression, most likely due to the impending structural phase transition to the *B2*-phase at 26.8 GPa [*Li and Jeanloz,* 1987], but returns at 8.3 GPa on decompression; we see no evidence of hysteresis in the velocities.

Our results closely match the aggregate average of *Whitfield et al.*'s [1976] single-crystal Brillouin scattering measurements, and are more consistent with *Birch*'s [1978] Eulerian rather than Lagrangian finite-strain analysis of NaCl elasticity (Figure 3.1). There is a systematic difference with respect to *Frankel et al.*'s [1976] data, however, as is most evident for the shear velocity at high pressure. As we show below, our results are compatible with the other data underlying *Birch*'s [1978] equation of state (notably, *Fritz, et al.*'s [1971] shock-wave measurements and *Spetzler, et al.*'s [1972] low-pressure ultrasonic results on single crystals), so we conclude that there may be a bias in *Frankel et al.*'s [1976] results (e.g., an error of 0.2 mm in their specimen thickness could account for the offset from our measurements; also, errors in pressure calibration are not considered in their work).

Due to anisotropy, a single crystal exhibits a sinusoidal variation in the velocity as a function of rotation about the laser beam axis, whereas a randomly oriented polycrystal should lack this variation at any given pressure (assuming a grain size smaller than the diameter of the laser-beam probe). We do find some variation in V_p and V_s with rotation about the laser beam axis, but it does not follow a sinusoidal trend and can be explained as being due to less-than-random sampling of crystal orientations (Figure 3.2a); similarly, there is some variation in velocities with position across the sample (Figure 3.2b).

Each measurement has accuracy at the percent level. The scatter in velocities at a given pressure seen in Figure 3.1 is thus not due to experimental uncertainty, but instead reflects orientation dependence of the velocities and, to a more limited extent, pressure variations across the non-hydrostatically loaded sample. This conclusion is supported both by the orientation-dependence of velocities at a given point – effectively, at a single pressure – in the sample (chi rotation, Figure 3.2a), and by comparing the velocity variations against the (modest) pressure variations measured across the sample (Figure 3.2b). Multiple or broad Brillouin peaks also indicate that many crystal orientations are being probed in our measurements.

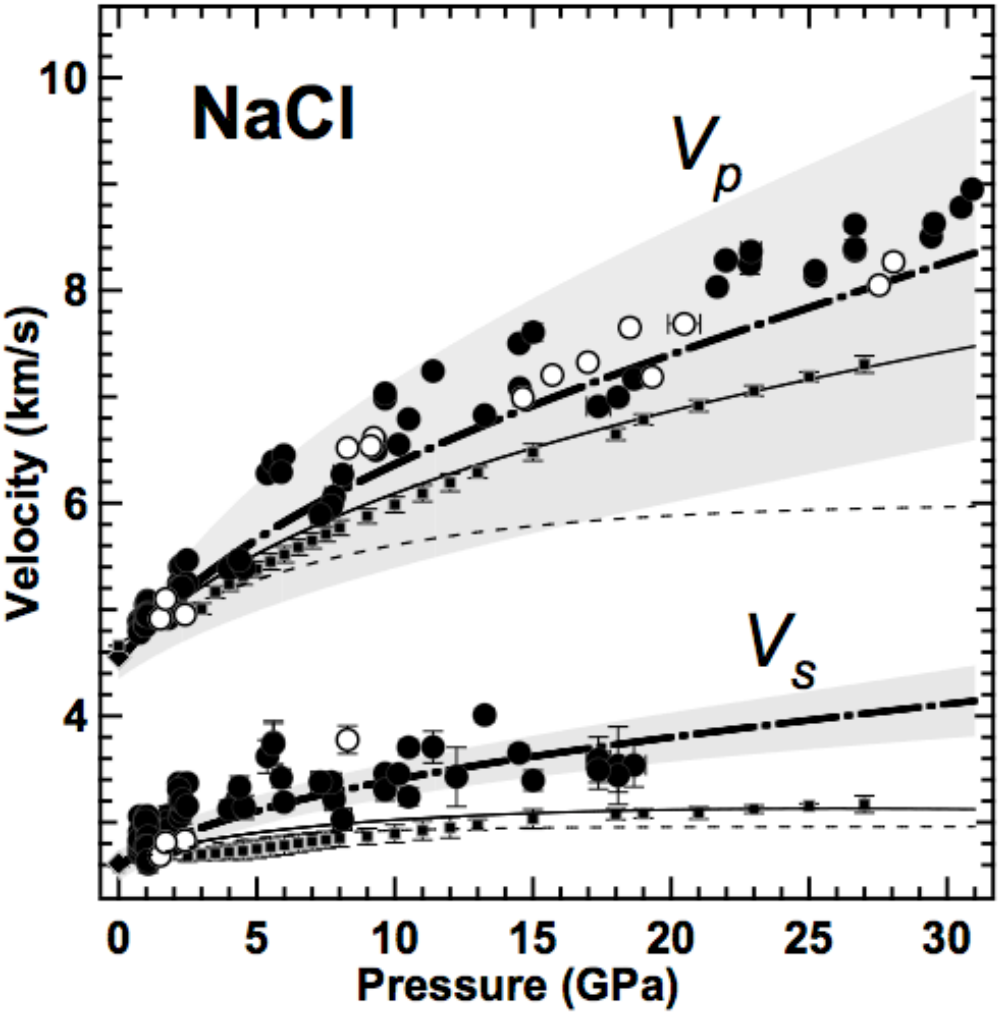

Figure 3.1: Compressional (V_P) and shear-wave (V_S) velocity measurements from the present study (circles, solid and open were collected in equal-angle scattering geometry on compression and decompression, respectively) are compared with single-crystal Brillioun data of *Whitfield et al.* [1976] (grey shading indicating uncertainty envelope) and polycrystalline ultrasonic data of *Frankel et al.* [1976] (small squares with error bars) at high pressures. Single-crystal ultrasonic data of *Spetzler et al*. [1972] at low pressures (diamonds), and *Birch*'s [1978] Eulerian (thin solid line) and Lagragian (thin dashed line) finite-strain analyses are indicated along with fits to our measurements (heavy dash-dot lines). All results shown here are at room temperature.

Collecting spectra in two geometries, we determine shear and compressional wave velocities as well as *n* as a function of pressure [*Shimizu et al.,* 1998; *Sasaki et al.,* 2009], obtaining the refractive index from $n(P) = (\omega_{180}(P)/\omega_{70}(P))sin(35^o)$. The zero pressure, room-temperature refractive index is fixed at 1.544 (at wavelength 589 nm, *Weast* [1979]), and we find that it increases smoothly to 1.81 (± 0.10) over by 22 GPa (Figure 3.3).

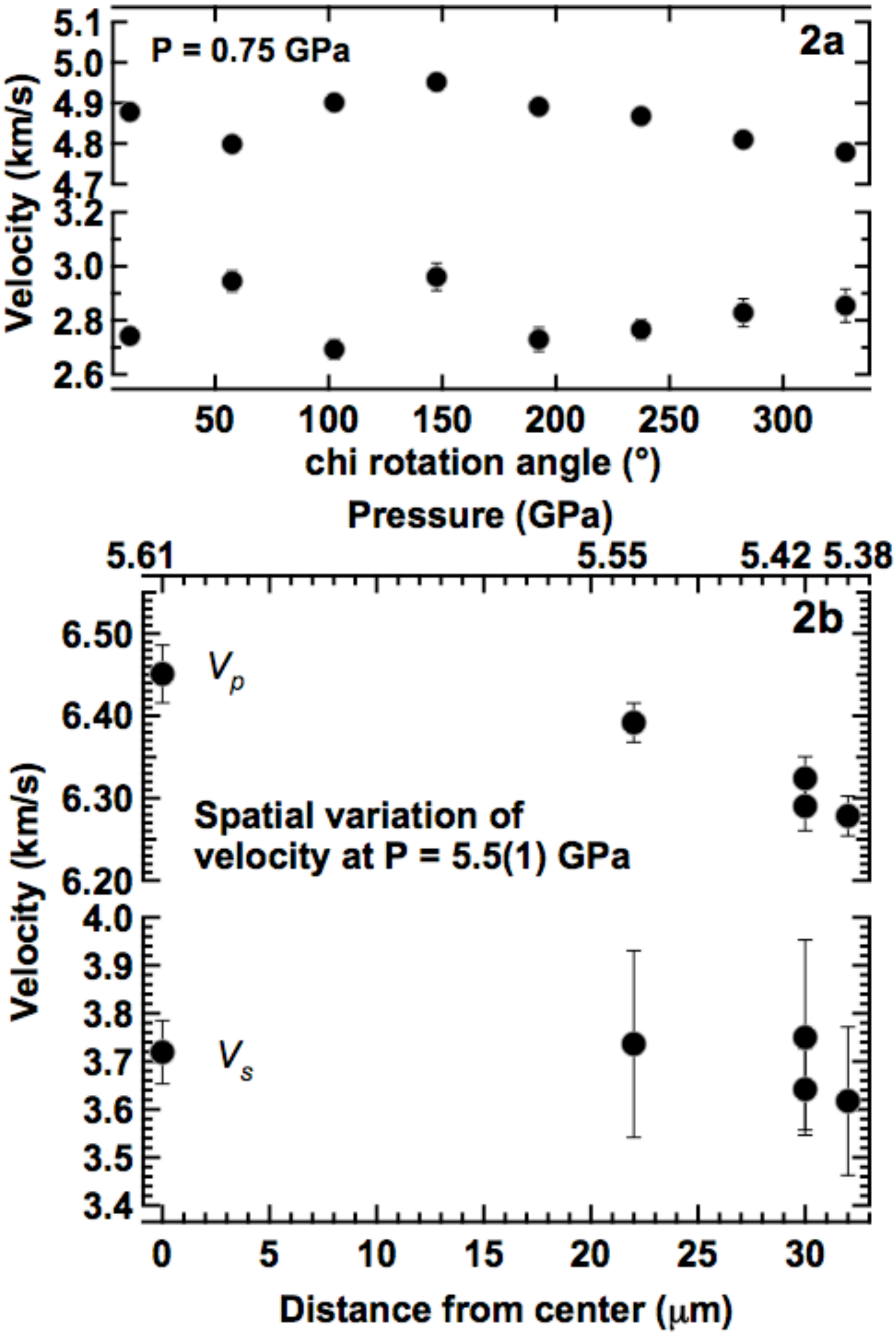

Figure 3.2a & b: Rotation dependence of measured velocities for polycrystalline NaCl shows scatter but no systematic sinusoidal variation (*a*). Velocities do show smaller systematic variations with position, presumably due to non-hydrostatic stress conditions (no pressure medium) (*b*).

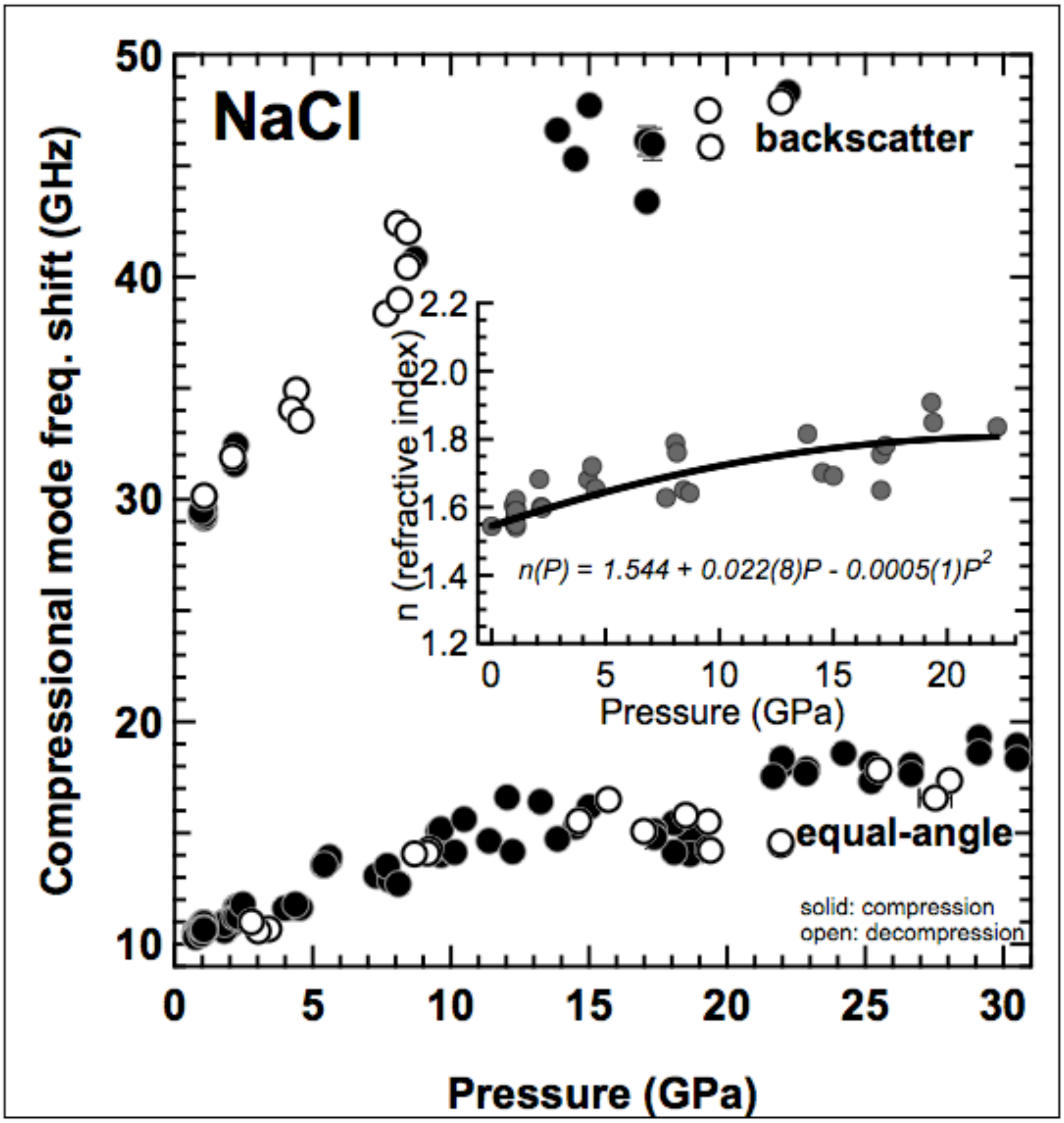

Figure 3.3: Compressional-mode Brillouin data for two scattering geometries, backscattering (θ = 180°) and equal-angle (θ = 70°), with solid and open symbols showing results collected on compression and decompression, respectively. *Inset:* Index of refraction determined as a function of pressure from the two sets of measurements (grey circles; black curve is the best fit polynomial).

We find the average isotropic elastic moduli from the measured compressional (V_p) and shear (V_s) wave velocities by $K_s = \rho\left(V_p^2 - 4V_s^2/3\right)$ and $G = \rho V_s^2$, where ρ, K_s and G are the density, adiabatic bulk and shear modulus, respectively. To compare these results with isothermally collected data, we employ $K_s = (C_p/C_v)K_T = \rho(C_p/C_v)(dP/d\rho)$, where C_p/C_v is the ratio of isobaric to isochoric specific heat. By definition, $\frac{C_p(P)}{C_v(P)} = 1 + \alpha(P)\gamma(P)T$, where α and γ are the pressure dependent thermal expansion and Grüneisen parameter, respectively. Using data provided by *Spetzler et al.* [1972], we find that $\log(\alpha\gamma T)$ is linearly related to $\log\left(\frac{\rho}{\rho_0}\right)$ and replace the ratio of specific heats with an expression solely dependent on ρ/ρ_0 (subscript zero indicates zero-pressure conditions). We integrate $d\rho / dP = (C_p / C_v)/(V_p^2 - 4V_s^2/3)$ to determine the density as a function of pressure (Figure 3.4).

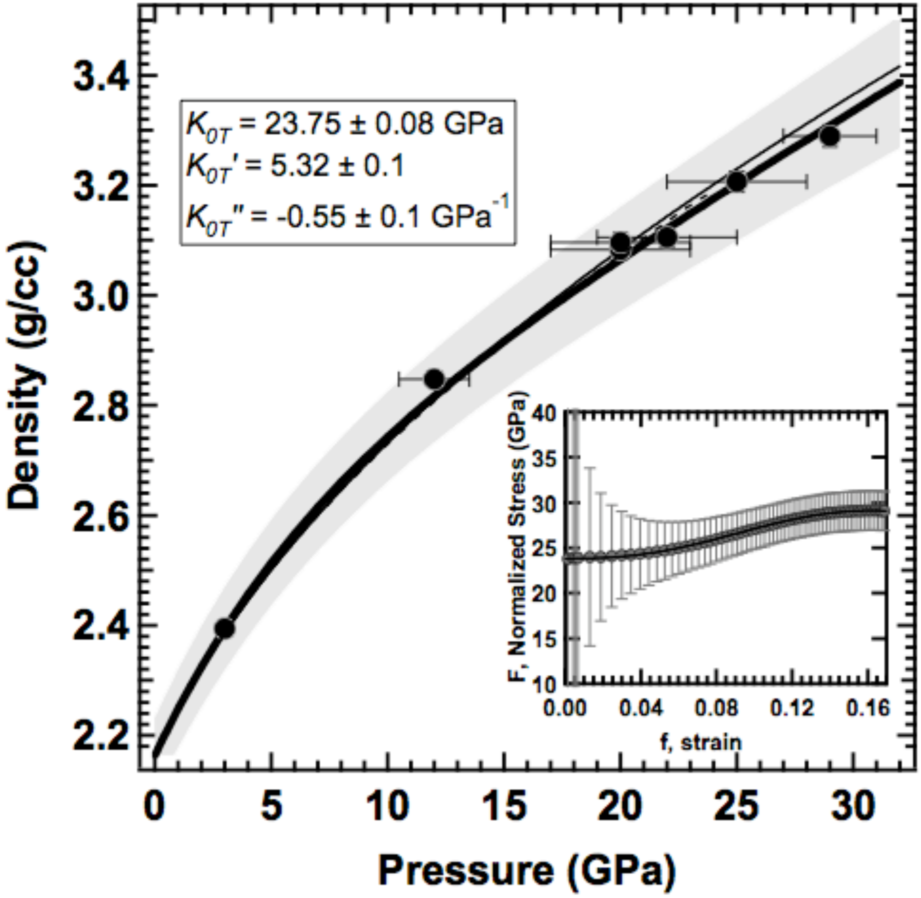

Figure 3.4: Density as a function of pressure obtained from integrating the Brillouin velocity measurements (thick solid black line, grey shaded area is uncertainty envelope: see text) is compared with *Birch*'s [1978] results (thin black line) based on ultrasonic [*Spetzler et al.*, 1972] and shock-wave [*Fritz et al.*, 1971] data. X-ray diffraction measurements (black circles: *Sato-Sorensen* [1983]) and a more recent analysis by *Brown* [1999] (dashed black line) are also shown. *Inset:* Normalized pressure ($F = P/[3f(1 + 2f)^{5/2}]$) vs. strain (f) as defined by *Birch* [1978] gives the zero-pressure values for the bulk modulus (K_0) and its pressure derivatives (see *Heinz and Jeanloz* [1984] for error analysis).

We use a finite-strain approach to analyze the results [*Birch*, 1978], but in order to maintain thermodynamic self-consistency, one must retain all terms in the elastic constants and pressure that originate from the same order in the expansion of free energy in strain [*Stixrude and Lithgow-Bertelloni,* 2005]. *Birch* [1978] derived a formula for the bulk modulus with pressure (his Eqn. 10) that does not retain all the necessary terms, so we revise his expression keeping all cubic terms (see the Appendix):

$$K_{general}(P) = K_0(1+2f)^{5/2}[1-5f+3fK_0'+\left(35/2\right)f^2-18f^2K_0'+\left(9/2\right)f^2K_0K_0'' + \left(9/2\right)f^2(K_0')^2+\left(1573/6\right)f^3+\left(59/6\right)f^3K_0K_0''+\left(33/2\right)f^3(K_0')^2-\left(231/2\right)f^3K_0'] \quad (3.1)$$

Here, prime indicates a pressure derivative, and the Eulerian strain measure f depends on the ratio of compressed to zero-pressure density,

$$f = \frac{1}{2}\left[\left(\frac{\rho}{\rho_0}\right)^{2/3} - 1\right]. \quad (3.2)$$

Our resulting equation of state gives K_{0T} = 23.75 (± 0.08) GPa, K_{0T}' = 5.32 (± 0.1) and K_{0T}'' = - 0.55 (± 0.1) GPa^{-1}, which agrees well with x-ray diffraction measurements [*Sato-Sorensen*, 1983], and the analyses of *Birch* [1978] (K_{0T} = 23.84 GPa, K_{0T}' = 5.35, and K_{0T}'' = -0.46 GPa^{-1}) and *Brown* [1999] (Figure 3.4). An assessment of our $V_s(P)$ data give a shear modulus G_0 = 14.9 (± 0.5) GPa (Figure 3.5), similar to *Birch*'s [1978] G_0 = 14.7 GPa using the *Peresada* [1971] method. Also, we find a pressure derivative of the shear modulus G_0' = 2.6 (± 0.5) comparable to the Voigt bound within our uncertainty.

This agreement between our Brillouin scattering data and independent experiments illustrates the utility of high-pressure Brillouin spectroscopy for characterizing the elasticity of polycrystalline materials.

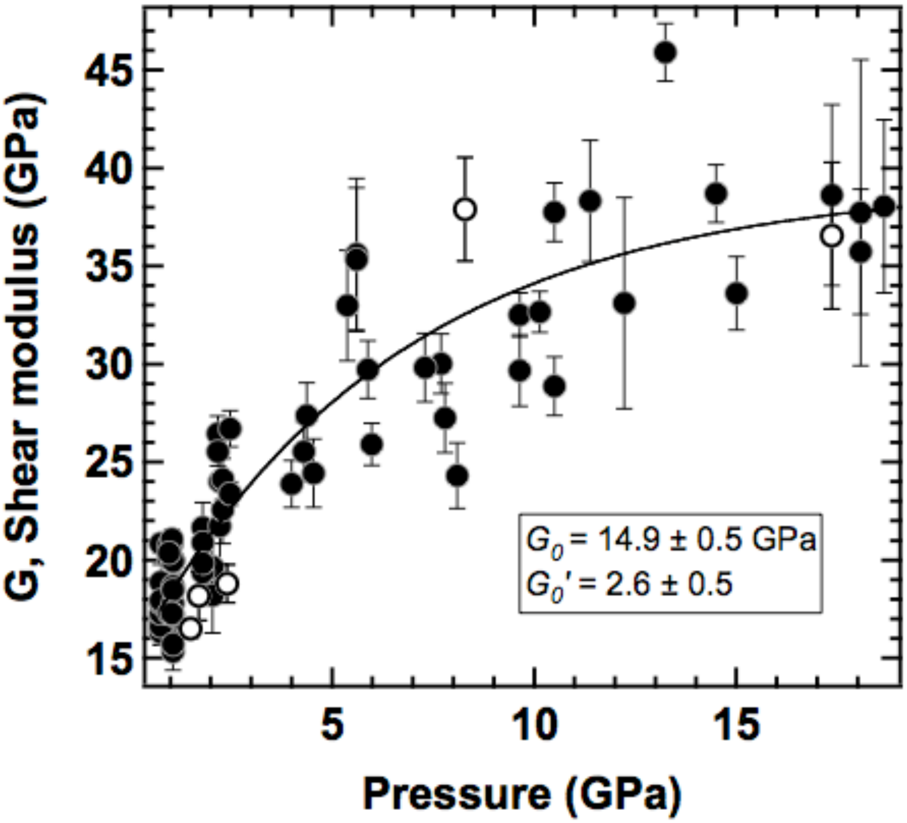

Figure 3.5: Shear modulus with pressure derived from the Brillouin measurements ($V_s^2 = G/\rho$ for an isotropic aggregate) are fitted to a polynomial, yielding coefficients that determine G_0 and G_0'.

Bibliography

Dil, J. (1982), Brillouin scattering in condensed matter, *Rep. Prog. Phys., 45*, 285 – 334.

Birch, F. (1978), Finite strain isotherm and velocities for single-crystal and polycrystalline NaCl at high pressures and 300°K. *J. Geophys. Res., 83*, 1257 – 1268.

Brown, M. (1999), The NaCl pressure standard, *J. Appl.Phys., 86*(10), 5801 – 5808.

Campbell, A., and D. Heinz (1992), A high-pressure test of Birch's law, *Science, 257,* 66-68.

Chen, B., et al. (2010), Elasticity, strength, and refractive index of argon at high pressure, *Phys. Rev. B, 81*, 144110, doi: 10.1103/PhysRevB.81.144110.

Decker, D.L., et al. (1972), High pressure calibration: a critical review, *J. Phys. Chem. Ref. Data, 1,* 773 – 835.

Frankel, J., et al. (1976), Acoustic velocities in polycrystalline NaCl at 300°K measured at static pressures from 25 to 270 kbar. *J. Geophys. Res., 81,* 6357 – 6363.

Fritz, J., et al. (1971), The Hugoniot equation of state of sodium chloride in the sodium chloride structure, Accurate characterization of the high-pressure environment, *Nat. Bur. Stand. U.S. Spec. Publ., 326,*201 – 208.

Gleason, A.E., et al. (2009), Grain-boundary effects in Brillouin scattering at ambient and high pressure, *Geophys. Res. Lett., 36*, L23309, doi:10.1029/2009GL040420.

Heinz, D., and R. Jeanloz (1984), The equation of state of the gold calibration standard, *J. Appl. Phys., 55*(4), 885 – 893.

Li, X., and R. Jeanloz (1987), Measurement of the B1-B2 transition pressure in NaCl at high temperatures. *Phys. Rev. B, 36*, 474 – 479.

Marquardt, H., et al. (2009), Single-crystal elasticity of $(Mg_{0.9}Fe_{0.1})O$ to 81 GPa, *Earth Planet. Sci. Lett., 287,* 345 – 352, doi:10.1016/j.epsl.2009.08.017.

Murakami, M., et al. (2007), Sound velocity of MgSiO3 perovskite to Mbar pressure, *Earth Planet. Sci. Lett., 256*, 47 – 54.

Murakami, M., et al. (2009), Elasticity of MgO to 130 GPa: implications for lower mantle mineralogy, *Earth Planet. Sci. Lett., 277*, 123 – 129, doi:10.1016/j.epsl.2008.10.010.

Peresada, G. (1971), On the calculation of elastic moduli of polycrystalline systems from single crystal data. *Physica Status Solidi (a), 4*, K23 – K27.

Sasaki, S., et al., (2009), High-pressure Brillouin study of the elastic properties of rare-gas solid xenon at pressures up to 45 GPa, *J. Raman Spect., 40*(2)*,* 121 – 127.

Sato-Sorensen, Y. (1983), Phase transitions and equations of state for sodium halides: NaF, NaCl, NaBr, and NaI, *J. Geophys. Res., 88*(B4), 3543 – 3548.

Shimizu, H., et al. (1998), High-pressure elastic properties of liquid and solid krypton to 8 GPa, *Phys. Rev. B. 57,* 230 – 233.

Spetzler, H., et al. (1972), Equation of state of NaCl: Ultrasonic measurements to 8 kbar and 800°C and static lattice theory, *J. Phys. Chem. Sol., 33*, 1727 – 1750.

Stixrude, L., and C. Lithgow-Bertelloni (2005), Thermodynamics of mantle minerals – I. Physical properties, *Geophys. J. Int., 162,* 610 – 632.

Weast, R.C. (1979), CRC Handbook of Chemistry and Physics 59th Edition, CRC Press Inc., Boca Raton, Florida. ISBN 0-8439-0459-8.

Whitfield, C.H., et al. (1976), Elastic moduli of NaCl by Brillouin scattering at high pressure in a diamond anvil cell. *Rev. Sci. Instr., 47*, 942 –947.

Chapter 4

Low sound velocities in polycrystalline MgO under non-hydrostatic compression

Brillouin scattering of non-hydrostatically compressed and decompressed polycrystalline MgO (periclase) to 60 GPa documents shear- and compressional-wave velocities ~20% lower than the Voigt-Reuss-Hill average values calculated from measurements on hydrostatically compressed single crystals. Calculations on the effects of non-hydrostaticity reveal that the sound wave velocities can be lowered, however, the calculated magnitude cannot explain our observations. We discuss possible additional causes for these anomalously low velocity trends, including grain size, grain boundary effects, preferred orientation, and impurities.

The study of elasticity of Earth materials has become increasingly important over the last decade, as contributions from global seismic tomography, seismological investigations of geographically and radially localized regions, mantle discontinuities, and analysis of normal modes of oscillations have revealed the Earth's mantle in unprecedented detail [e.g., *Ishii and Tromp*, 1999]. High pressure single-crystal Brillouin spectroscopy is routinely used to measure acoustic-wave velocities [e.g., *Whitfield et al.,* 1976]. So far, Brillouin scattering results on single-crystals have been reported to 81 GPa [*Marquardt et al*., 2009a], whereas measurements on polycrystals reached more than twice that pressure [*Murakami et al.,* 2007]. Previous studies have illustrated the suitability of polycrystalline Brillouin spectroscopy for extracting average acoustic-wave velocities [e.g., *Campbell and Heinz*, 1992; *Murakami et al*., 2009, *Gleason et al.,* 2009; *Chen et al*., 2010].

Non-hydrostaticity can significantly affect measured lattice parameters of materials [e.g., *Funamori et al*., 1997; *Fei,* 1999]. However, the effect of non-hydrostatic stress on the propagation of sound waves in minerals and therefore seismic velocities, has not been well explored. *Watts* [1978] and *Kanamori* [1980] document stresses of several tenths of a GPa in the lithosphere due to topography alone. Large stress drops, 0.2 – 0.5 GPa, determined from earthquakes in the crust down to the transition zone may provide a lower bound to non-hydrostatic stresses [e.g., *Kanamori* 1980; *Chung and Kanamori*, 1980; *Munguia and Brune*, 1984; *Fukao and Kikuchi*, 1987; *Kanamori et al.,* 1998]. Furthermore, the process of calculating a stress drop is model dependent, where values can vary up to an order of magnitude depending on the model; the Brune-type, used most frequently, provides the lowest estimate [*Ruff*, 1999; D. Dreger, 2010, *personal communication*]. Also, plate-bending models [e.g., *Conrad and Hager*, 1999; *Buffet*, 2006; *Kaus et al*., 2009] show that average fault stresses can reach 0.25 GPa. Here we look at the case study of MgO compressed hydrostatically and non-hydrostatically exploring the effects of these stress states on the seismic velocities using polycrystalline Brillouin scattering.

(Mg,Fe)O is expected to coexist with Mg-rich and Fe-, Ca- and Al-bearing silicate perovskite in the Earth's lower mantle [*Jacobsen et al*., 2002] with ferropericlase being potentially the most abundant non-silicate oxide in the Earth [*Bina*, 1998]. Measurements of the elastic properties of (Mg,Fe)O may provide constraints on the composition of the lower mantle. However, as iron introduces complexities, such as high-spin vs. low-spin states and site occupancy variability in the crystal structure, which can affect the elasticity [*Crowhurst et al.,* 2008; *Marquardt et al*., 2009b], we choose to begin with the simple end-member MgO.

MgO (periclase) is an archetypal oxide with the NaCl-type (B1) crystal structure ($Fm\bar{3}m$). We use three initial sample types: 1) MgO powder ground to 5-10 μm grain size (Mallinckrodt, Analytical reagent #6015, 99.3% purity), 2) 1 μm grain size powder MgO (American Elements, MG-OX-03-P, 99.9% purity), and 3) 6 μm average grain size sintered translucent MgO [*Chen et al.,* 2008].

For non-hydrostatic loading, a stainless steel gasket pre-indented to a final thickness of 50 μm with a 130 μm hole serves as the pressure chamber using 300 μm culet diamonds in a short symmetric cell (G. Rose, Princeton University). Initially, powder is placed on bare culets and gently pressed together to form a semi-transparent disc of ~50 μm thickness on one culet face. After decompression, radial cracks form in the MgO similar to *Meade and Jeanloz* [1988] (their Figure 6b). On the opposite culet 5 - 8 ruby spheres, each < 1 – 2 μm in diameter, are distributed across the chamber to monitor pressure [*Mao et al*., 1978]. The hole in the gasket slices the polycrystalline MgO disc in a cookie-cutter fashion when the cell is closed.

A similar procedure is followed for non-hydrostatically loading the 6 μm sintered MgO. The original sintered polycrystalline wafer (450 μm thick) is polished on both sides down to 50 μm. In addition, for a separate run, the 6 μm sintered MgO was polished to 30 μm, sliced to a 75 x 75 μm square and loaded quasi-hydrostatically in a 50 μm thick gasket plus ruby spheres and 4:1 methanol:ethanol (ME) mixture as the pressure transmitting medium.

At each pressure, Brillouin spectra were collected in transmission geometry using 0.50 W of polarized 532 nm radiation from a continuous-wave Nd:YVO_4 laser, along with a Sandercock six-pass tandem Fabry-Perot interferometer. For equal-angle transmission (scattering angle θ) with a parallel-sided platelet sample, ω is the measured frequency shift, λ_0 is the incident laser wavelength, and the wave velocity (V) for a shear ($_s$) or compressional ($_p$) mode is given by $V_{s,p} = (\omega)\lambda_0 / 2\sin(\theta/2)$.

Brillouin spectra from non-hydrostatically loaded pressed powder samples and hydrostatically loaded pre-sintered polycrystalline MgO wafers are measured in compression and decompression. Each spectrum is folded about the central Rayleigh peak to enhance the Brillouin signal from the sample [*Gleason et al.*, 2009]. Gaussian peak fits are applied to extract acoustic velocities. Using three different starting materials, we completed several pressure cycles on non-hydrostatically loaded samples up to a maximum pressure of 60 GPa. Mode assignment for the non-hydrostatic case (only MgO and ruby spheres in the sample chamber) was straightforward – with two modes, the higher frequency shift is assigned the compressional mode, and the lower frequency shift is the shear mode.

Pre-sintered MgO [*Chen et al.,* 2008] loaded quasi-hydrostatically in 4:1 methanol:ethanol was measured under compression and decompression up to 15 GPa (largest circles, Figure 4.1; upper most trace of inset). Here we see no evidence of ME peaks in any of the Brillouin spectra, including at pressures where the ME compressional mode would stand alone [*Armstrong et al.,* 2008], so we assume no contamination of ME modes in our spectra. Ruby spheres did not give a Brillouin signal.

We find that the data match the hydrostatic single crystal aggregate average trends (smaller circles, Figure 4.1) [*Bogardus*, 1965; *Spetzler,* 1970; *Jackson and Niesler*, 1982; *Sinogeikin and Bass*, 2000]. Quasi-hydrostatic polycrystalline MgO data from *Murakami et al.* [2009] (crosses, Figure 4.1) loaded in NaCl, also match this trend. The Voigt (uniform strain) and Reuss (uniform stress) averaging schemes are the maximum and minimum limits, respectively, for a randomly oriented polycrystal, with closer bounds developed by Hashin and Shtrikman [*Schreiber, et al.,* 1973]. Using the elastic constants and pressure derivatives (c_{ij}, c_{ij}', c_{ij}'') provided by each study, *Sinogeikin and Bass* [2000]; *Jackson and Niesler* [1982]; *Bogardus* [1965], we calculate curves for the Voigt, Reuss, and Hashin-Shtrikman bounds for each single crystal data set: black and grey curves in Figure 4.1 [*Bateman et al.*, 1961; *Simmons and Wang*, 1971; *Birch*, 1978].

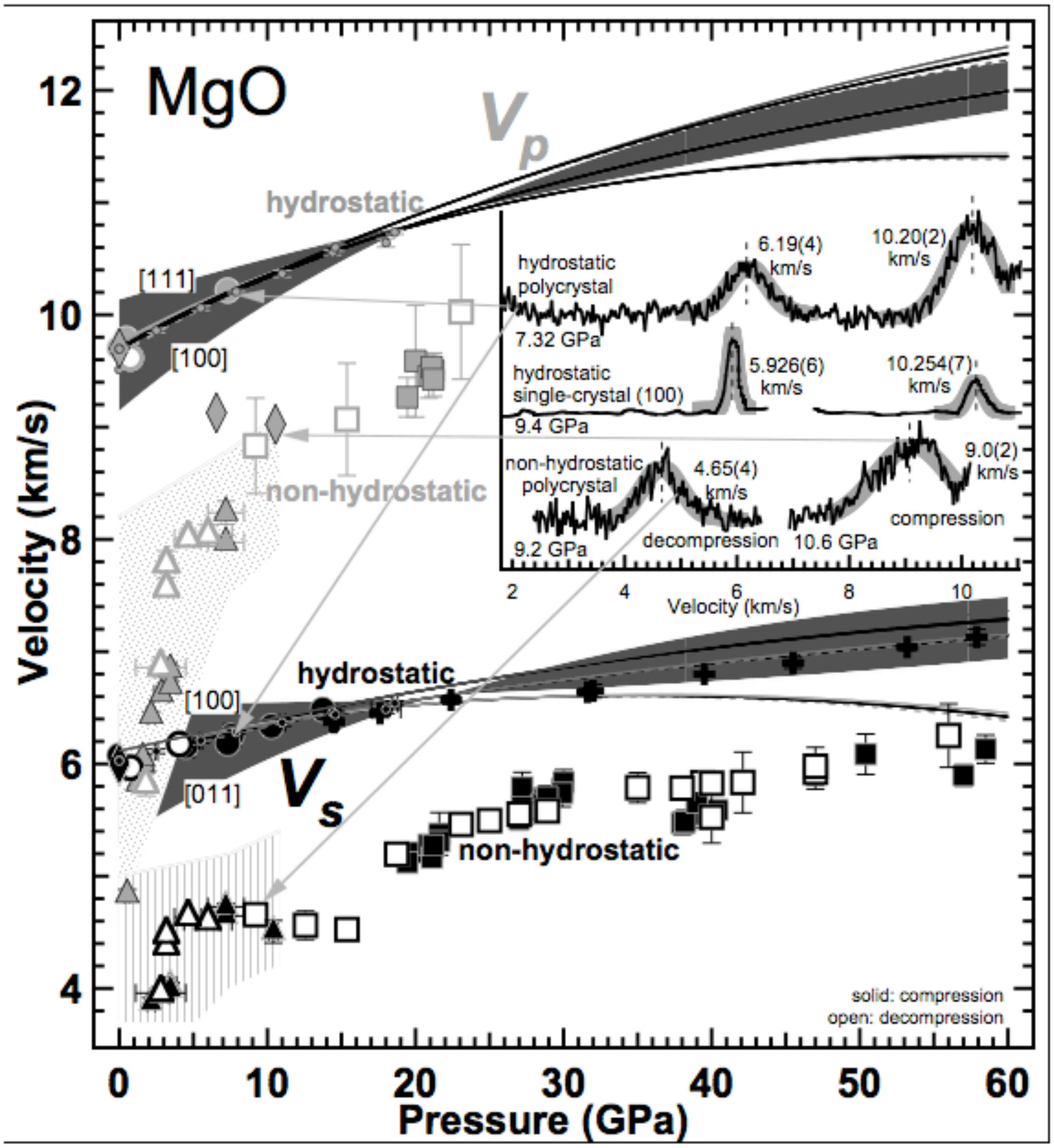

Figure 4.1: Comparison of our non-hydrostatically loaded MgO to hydrostatically loaded single- and poly-crystals. All grey symbols are compressional wave speeds (V_p) and black symbols are shear wave speeds (V_s); solid symbols are compression and open are decompression. The following are non-hydrostatically loaded polycrystals: squares are 5-10 μm pressed powder; triangles are 1 μm pressed powder; diamonds are 6 μm sintered. The largest circles are hydrostatically loaded, sintered MgO wafers loaded in methanol:ethanol mixture. Small circles are aggregate averages calculated from single-crystal constants measured by *Sinogeikin and Bass* [2000] and *Spetzler* [1970] by Brillouin scattering and ultrasonic interferometry, respectively. Black crosses are hydrostatically loaded polycrystalline MgO platelets [*Murakami et al.,* 2009]. The range of brucite velocities are shaded regions [*Jiang et al.,* 2006], grey dotted area is V_p basal maximum to meridian minimum, and grey hatched area is V_s basal maximum to minimum. A trio of averaging schemes, Voigt (solid upper bound), Reuss (lower dashed bound) and Hashin-Shtrikman (solid inner two black curves), are provided for single crystal datasets: *Bogardus* [1965] (upper-most trio of curves for V_p and V_s), *Sinogeikin and Bass* [2000] (middle), and *Jackson and Niesler* [1982] (lower-most). This indicates our non-hydrostatic data are consistently below the Reuss bound, regardless of dataset used. Inset graph shows trace profiles for hydrostatically and non-hydrostatically loaded samples at nearly the same pressure (7 - 10 GPa, compression and decompression) for our polycrystalline sample, and for a hydrostatically loaded single crystal of $(Mg_{0.987},Fe_{0.013})O$ [100] (*Reichmann et al.* [2008], their Figure 1b, Figure 2b). Some non-hydrostatic polycrystal traces on compression and decompression respectively show only V_p or V_s due to the combination of incident and scattered light polarizations and/or overlap of p-mode with the diamond shear-mode. The Rayleigh peak and diamond shear mode are removed; similarly, the methanol-ethanol-water peak has been removed from the single-crystal trace. Dark grey shaded area indicates the range of single crystal absolute maximum and minimum V_s and V_p for a given (listed) orientation as determined by using pressure dependent c_{ij} values from *Sinogeikin and Bass* [2000] and the expressions for acoustic velocity in specific crystal directions provided by *Schreiber et al.* [1973].

Surprisingly, *all* non-hydrostatically loaded samples exhibit ~20% lower velocities (triangles, squares, and diamonds at pressure, Figure 4.1) than hydrostatically loaded aggregate averaged single-crystals and polycrystals. For pressed powder data, we observe from 0 – 10 GPa extreme low shear and compressional wave speeds, 2 – 3 km/s below the expected values for a MgO aggregate at ambient conditions. At roughly 10 GPa, there is a change in the pressure dependence of the velocities for both V_s and V_p; between 10 – 60 GPa (compression and decompression of pressed powder) the velocity trend is nearly sub-parallel to the hydrostatic single crystal aggregate trend (bottom most trace, Figure 4.1 inset). For example, after compressing to 60 GPa and then decompressing down to 35 GPa, we see a mode at 12.5 GHz, equivalent to 5.8 (±0.1) km/s, which we interpret to be the MgO shear mode at ~15% lower than the expected single crystal average at 6.8 km/s (determined using aggregate elastic moduli and pressure derivatives provided by *Sinogeikin and Bass* [2000], their Table 4). No compressional mode is seen here due to the superposition of the diamond shear mode. We also note the peak profiles for polycrystalline data are generally much broader, reflecting an average of crystallite orientations, compared to a single crystal profile at nearly the same pressure (middle trace, Figure 4.1 inset).

For pre-sintered MgO, velocities measured under non-hydrostatic compression up to 11 GPa (solid diamonds, Figure 4.1; top trace, Figure 4.2) are also low, comparable to pressed powder data at the same pressure. Figure 4.2 shows the position of the diamond V_s mode, the methanol:ethanol V_p mode (grey arrow) [*Armstrong et al.*, 2008] in the hydrostatic trace, indicating we have no mode superposition. Unlike the pressed powder, pre-sintered MgO has welded grains which minimize scatter due to inhomogeneous structure, possibly voids, and we record both shear and compressional velocities matching the single crystal average (solid diamonds at 0 GPa, Figure 4.1). With increasing non-hydrostatic pressure, the sintered wafer is crushed, so the environment of each crystallite is more like pressed powder, and we see the same low velocity trend begin to develop. Decompression measurements of the non-hydrostatic pre-sintered sample were not collected and after opening the cell at 0 GPa, the sample was no longer transparent or translucent, making it impossible to measure an ambient Brillouin spectrum in transmission geometry.

At each pressure, Brillouin spectra were collected at 4 – 8 locations evenly distributed around the sample chamber. Near these same locations within the sample chamber, the pressure was determined by way of ruby fluorescence, providing an estimate of pressure gradients across the sample. The sample thickness prior to compression is estimated to be the thickness of the pre-indention in the gasket, 50 μm. After decompression the gasket is removed from the diamond-cell and the new thickness is measured with a micrometer to be 10 μm. The pressure gradient combined with a measure of the sample thickness before and after decompression allows for a calculation of the shear stresses [*Meade and Jeanloz*, 1988], (Figure 4.3). We can correlate these shear stresses, normalized by the measured pressure, with the measured velocity differences (as seen in Figure 4.1) between the hydrostatic single crystal aggregate average and the non-hydrostatic trends (plotted as inset in Figure 4.3). As the normalized shear stress increases over the whole pressure range (0 - 60 GPa), the normalized velocity difference also increases.

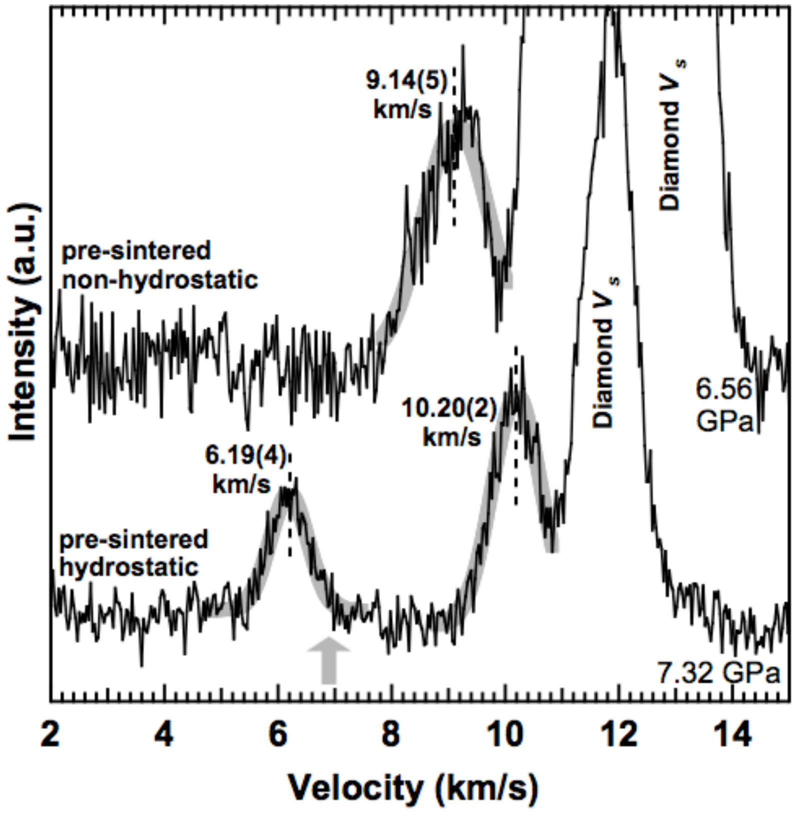

Figure 4.2: Hydrostatic and non-hydrostatic Brillouin scattering traces (black) of pre-sintered polycrystalline MgO at ~7 GPa. Grey curves are Gaussian fits with peak centers (dashed black line). Labeled are the diamond shear modes, and the methanol:ethanol V_p mode (grey arrow) in the hydrostatic trace.

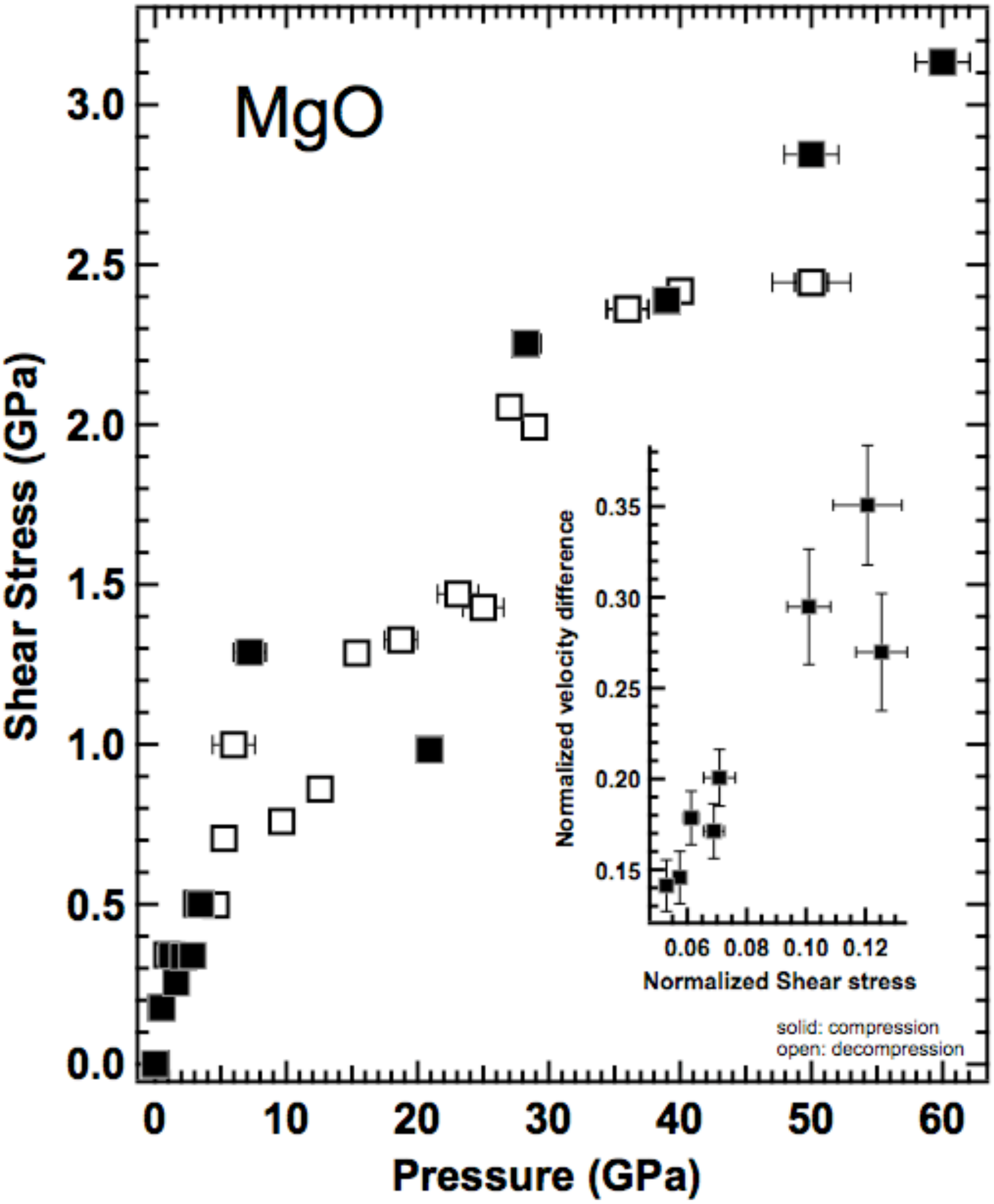

Figure 4.3: Maximum shear stress ($\sigma_{shearstress}$) in polycrystalline MgO calculated from $\frac{h}{2}\frac{dP}{dr} = \sigma_{shearstress}$, where h is the sample thickness, and dP/dr is the measured pressure gradient based on spatial distribution of ruby spheres. Based on this relationship between the shear stress and pressure, we plot the velocity difference of the shear mode (hydrostatic velocity - non-hydrostatic velocity normalized by the hydrostatic velocity) at the corresponding shear stress normalized by the measured pressure for a few selected points (inset plot).

Prompted by our observation that non-hydrostatically loaded polycrystalline MgO velocities are substantially lower than the predicted averages under hydrostatic loading, we calculate sound velocities (Figure 4.4) in terms of second- and third-order elastic constants for shear and compressional modes in uniaxially compressed cubic crystals. Uniaxial compression serves here as a proxy for non-hydrostatic stress applied to a cubic single crystal. We first determine the compressional and two shear velocities in the [001] and [110] for hydrostatic compression of a single crystal. The pressure dependent c_{ij}'s [*Sinogeikin and Bass*, 2000], density [*Speziale et al.,* 2001] and experimental third order elastic constants [*Bogardus,* 1965] give compressional and shear velocities in [001] and [110] directions [*Mason,* 1968]. These pressure dependent velocity trends under hydrostatic conditions (solid curves, Figure 4.4) are compared to the non-hydrostatic case.

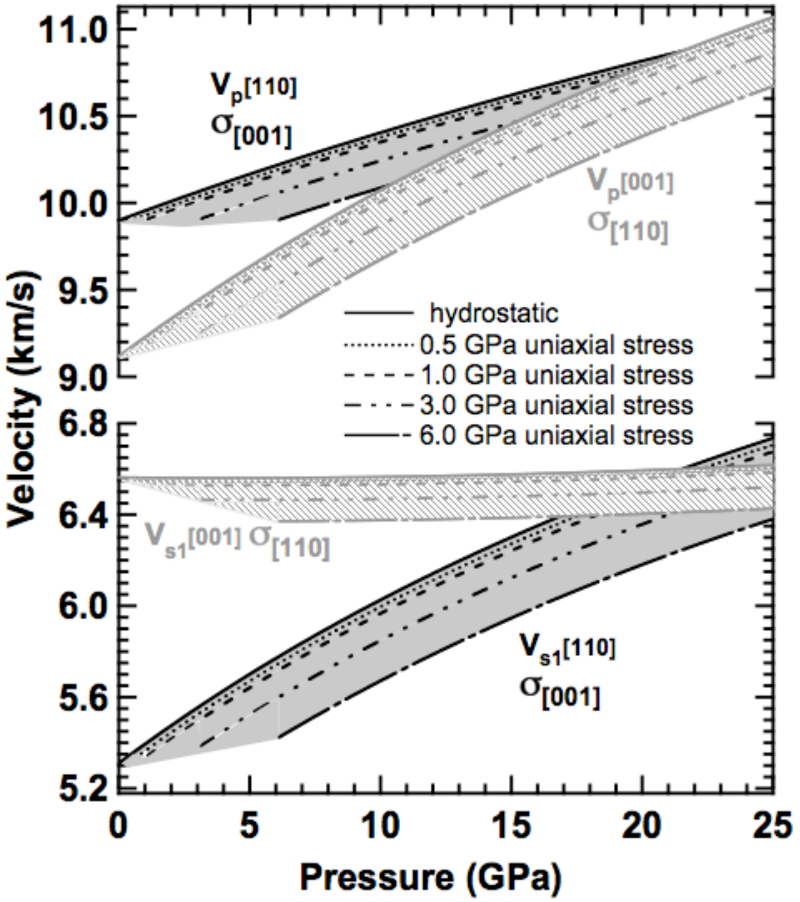

Figure 4.4: Calculated compressional (*P*) and shear (*S*) velocity trends for single-crystal MgO along the [001] and [110] crystallographic directions; the hydrostatic case (solid line) is compared with different values of applied uniaxial stress (σ) (all dashed curves) as a proxy for non-hydrostatic stress conditions in the diamond-anvil cell.

The velocity in a specified crystal direction is affected by imposing oriented uniaxial compression (applying non-hydrostatic stress) as expressed by *Bateman et al.,* [1961], their Tables II, and III. For each imposed non-hydrostatic stress state we choose (i.e., 0.5, 1.0, 3.0 or 6.0 GPa as the amount of uniaxial compression), the difference between the velocity under hydrostatic and non-hydrostatic conditions is determined and applied to the pressure-dependent trend (all dashed curves, Figure 4.4); we find a 7% drop, at most. Based on these calculations, it does not seem possible that the tens of percent velocity deviations we observe for non-hydrostatically compressed MgO powder can be explained by the elastic effects of uniaxial stresses. The calculations indicate a velocity decrease in the plane perpendicular to the applied uniaxial stress for MgO, which corresponds to the plane that is probed by our Brillouin scattering experiments, but the magnitude of this effect alone cannot account for our observations.

Influences of texturing (preferred orientation) in monomineralic, polycrystalline MgO cannot account for low velocities in any pressure range. The magnitude of those effects as a function of pressure are, at most, ± ~6% about the aggregate average (shown by a spread of V_s and V_p as a function of single-crystal orientation at any given pressure [*Sinogeikin and Bass*, 2000; *Schreiber et al.*, 1973], dark grey envelope, Figure 4.1). It is interesting to note that MgO becomes nearly isotropic at ~20 GPa [*Sinogeikin and Bass,* 2000; *Marquardt et al.,* 2009b].

Also in our attempt to identify the cause of the anomalous velocities we consider the effect of impurities. MgO is hygroscopic, easily allowing formation of $Mg(OH)_2$ (brucite), much softer than MgO. If brucite contributes to the Brillouin signal, our measured velocities could be lower. We compare the maximum range of velocities for a single crystal of brucite [*Jiang et al.,* 2006] to our low MgO velocities (shaded regions from *Jiang et al.,* [2006] Figure 4.1, grey dotted area is V_p basal maximum to meridian minimum, and grey hatched area is V_s basal maximum to minimum) and see considerable overlap from 0 – 10 GPa. However, all samples used for Brillouin measurements (powder and sintered) were checked at ambient conditions for contamination using x-ray diffraction and Raman spectroscopy. No evidence of brucite was found by either technique.

A combination of mechanisms may act in concert to generate low velocities: 1) grain size decrease, 2) static grain size with Brillouin signal from amorphous grain boundaries. *Yeheskel et al.* [2005], using ultrasonic techniques, found the Young's and shear moduli of nanocrystalline MgO were lower by 13% than those with submicron grain size, indicating that a decrease in elastic moduli is directly related to an increase in the volume fraction of the grain boundaries. If the Brillouin signal is dominated by scattering from grain boundary material, then deformation mechanisms at the boundaries make it softer than crystalline cores, resulting in decreased sound velocity. However, grain fragmentation is not necessarily supported by our decompression trend, which traces back the same path, and these conditions and timescale make grain coarsening unlikely. Nevertheless, the effect of grain size and potential grain size reduction in Brillouin scattering experiments and the associated effects on the derived Brillouin frequency shifts need to be clarified in future studies [*Marquardt, et al.,* 2010, in preparation]. A deep understanding of these effects is essential for a reliable study of multigrain Earth materials, particularly where no single-crystal reference data sets are available.

Bibliography

Armstrong, M.R., et al. (2008), Ultrafast high strain rate acoustic wave measurements at high static pressure in a diamond anvil cell, *Appl. Phys. Lett., 92*, 101930.

Bateman, T., et al. (1961), Third-order elastic moduli of germanium, *J. Appl. Phys., 32*(5), 928 – 936, doi:10.1063/1.1736135.

Bina, C.R. (1998), Lower mantle mineralogy and the geophysical, in *Ultrahigh-Pressure Mineralogy: Physics and Chemistry of Earth's Deep Interior, Rev. Mineral.*, vol. 37, edited by R.J. Hemley, pp. 205 – 239, Mineral. Soc. Of Am., Washington, D. C.

Birch, F. (1978), Finite strain isotherm and velocities for single-crystal and polycrystalline NaCl at high pressure and 300^{o}K, *J. Geophys. Res., 83*(B3), 1257 – 1268.

Bogardus, E. (1965), Third-order elastic constants of Ge, MgO, and fused SiO2, *J. Appl. Phys., 36,* 2504 – 2513, doi:10.1063/1.1714520.

Buffet, B. (2006), Plate force due to bending at subduction zones, *J. Geophys Res., 11,* B09405.

Campbell, A.J., and D.L. Heinz (1992), A high-pressure test of Birch's law, *Science, 257*(5066), 66 – 68, doi: 10.1126/science.257.5066.66.

Chen, B., et al. (2010), Elasticity, strength, and refractive index of argon at high pressure, *Phys. Rev. B, 81*, 144110, doi: 10.1103/PhysRevB.81.144110.

Chen, D., et al. (2008), Pressureless sintering of translucent MgO ceramics, *Scripta Materialia, 59*, 757 – 759, doi:10.1016/j.scriptamat.2008.06.007.

Chung, W.-Y., and H. Kanamori (1980), Variation of seismic source parameters and stress drops within a descending slab and its implications in plate mechanics, *Phys. Earth Planet. Inter., 23*, 134 – 159.

Conrad, C.P., and B. Hager (1999), Effects of plate bending and fault strength at subduction zones on plate dynamics, *J. Geophys. Res., 104*(B8), 17551 – 17571.

Crowhurst, J.C., et al. (2008), Elasticity of (Mg,Fe)O through the spin transition of iron in the lower mantle, *Science, 319*, 451 – 453, doi: 10.1126/science.1149606.

Fei, Y. (1999), Effects of temperature and composition on the bulk modulus of (Mg,Fe)O, *Am. Min., 84*(3), 272 – 276.

Fukao, Y., and M. Kikuchi (1987), Source retrieval for mantle earthquakes by iterative deconvolution of long-period P-waves, *Tectonophyisics, 144*, 249 – 269.

Funamori, N., et al. (1997), Broadening of high-pressure x-ray powder diffraction lines under non-hydrostatic stress, *J. Appl. Phys., 82*(1), 142 – 146.

Gleason, A.E., et al. (2009), Grain-boundary effects in Brillouin scattering at ambient and high pressure, *Geophys. Res. Lett., 36*, L23309, doi:10.1029/2009GL040420.

Ishii, M., and J. Tromp (1999), Normal-mode and free-air gravity constraints on lateral velocity variations in velocity and density of Earth's mantle, *Science, 285*, 1231 – 1236, doi: 10.1126/science.285.5431.1231.

Jackson, I., and H. Niesler (1982), The elasticity of periclase to 3 GPa and some geophysical implications, in *High Pressure Research in Geophysics*, edited by S. Akimoto and M.H. Manghnani, pp. 93 – 113, Center Acad. Publ. Jpn., Tokyo.

Jacobsen, S.D., et al. (2002), Structure and elasticity of single-crystal (Mg,Fe)O and a new method of generating shear waves for gigahertz ultrasonic interferometry, *J. Geophys. Res., 107*(B2), 2037 - 2051, doi: 10.1029/2001JB000490.

Jiang, F., et al. (2006), Single-crystal elasticity of brucite, Mg(OH)2, to 15 GPa by Brillouin scattering, *Am. Min., 91*, 1893 – 1900, doi: 10.2138/am.2006.2215.

Kanamori, H. (1980), State of stress in the Earth's lithosphere, in *Physics of the Earth's interior, Proc, Int. Sch. Phys. 'Enrico Fermi',* edited by A.M. Dziewonski and E. Boschi, pp. 531 – 552, Amsterdam, North Holland.

Kanamori, H., et al. (1998), Frictional melting during the rupture of the 1994 Bolivian earthquake, *Science, 279,* 839 – 842, doi:10.1126/science.279.5352.839.

Kaus, B., et al. (2009), Lithospheric stress-state predicted from long-term tectonic models: Influence of rheology and possible application to Taiwan, *J. Asian Earth Sci., 36*, 119 – 134.

Mao, H.K., et al. (1978), Specific volume measurements of Cu, Mo, Pd, and Ag and calibration of the ruby R1 fluorescence pressure gauge from 0.06 to 1 Mbar, *J. Appl. Phys., 49*(6), 3276 – 3283, doi:10.1063/1.325277.

Marquardt, H., et al. (2009a), Single-crystal elasticity of ($Mg_{0.9}Fe_{0.1}$)O to 81 GPa, *Earth Planet. Sci. Lett., 287,* 345 – 352, doi:10.1016/j.epsl.2009.08.017.

Marquardt, H., et al. (2009b), Elastic shear anisotropy of ferropericlase in Earth's lower mantle, *Science, 324,* 224 – 226, doi: 10.1126/science.1169365.

Marquardt, H., et al. (2010), Grain size effects in Brillouin scattering, *in prep*.

Mason, W. (1958), *Physical acoustics and the properties of solids*, D. Van Nostrand Company, Inc., pp. 368 – 380, Princeton, New Jersey.

Meade, C., and R. Jeanloz (1988), Yield strength of MgO to 40 GPa, *J. Geophys. Res., 93*(B4), 3261 – 3269, doi:10.1029/JB093iB04p03261.

Munguia, L., and J. Brune (1984), High stress drop events in the Victoria, Baja California earthquake swarm of 1978 March, *Geophys. J. R. astr. Soc., 76*, 725 – 752.

Murakami, M., et al. (2007), Sound velocity of $MgSiO_3$ perovskite to Mbar pressure, *Earth Planet. Sci. Lett., 256*, 47 – 54, doi:10.1016/j.epsl.2007.01.011.

Murakami, M., et al. (2009), Elasticity of MgO to 130 GPa: implications for lower mantle mineralogy, *Earth Planet. Sci. Lett., 277*, 123 – 129.

Reichmann, H., et al. (2008), Single-crystal elastic properties of (Mg0.987,Fe0.013)O to 9 GPa, *Am. Min., 93*, 1306 – 1311, doi:10.2138/am.2008.2717.

Ruff, L.J. (1999), Dynamic stress drop of recent earthquakes: variations within subduction zones, *Pure Appl. Geophys., 154*, 409 – 431.

Schreiber, E., et al. (1973), *Elastic constants and their measurements*, McGraw-Hill Inc., pp. 25 – 31, New York, New York. ISBN 0-07-055603-2.

Simmons, G., and H. Wang (1971), *Single Crystal Elastic Constants and Calculated Aggregate Properties: A Handbook, 2nd Ed.,* The MIT Press, pp. 10 – 11, Cambridge, Massachusetts. ISBN-10: 0262190923.

Sinogeikin, S., and J. Bass (2000), Single-crystal elasticity of pyrope and MgO to 20 GPa by Brillouin scattering in the diamond cell, *Phys. Earth Planet. Int., 120,* 43 – 62.

Spetzler, H. (1970), Equation of state of polycrystalline and single-crystal MgO to 8 kilobars and 800°K, *J. Geophys. Res., 75*(11), 2073 – 2087.

Speziale, S., et al. (2001), Quasi-hydrostatic compression of magnesium oxide to 52 GPa: Implications for the pressure-volume-temperature equation of state, *J. Geophys. Res., 106*(B1), 515 – 528, doi:10.1029/2000JB900318.

Watts, A.B. (1978), An analysis of isostasy in the world's oceans 1. Hawaiian-Emperor seamount chain, *J. Geophys. Res., 83*(B12), 5989 – 6004.

Whitfield, C.H., et al. (1976), Elastic moduli of NaCl by Brillouin scattering at high pressure in a diamond anvil cell, *Rev. Sci. Instrum., 47*(8), 942 – 947.

Yeheskel, O., et al. (2005), Elastic moduli of grain boundaries in nanocrystalline MgO ceramics, *J. Mater. Res., 20*(3), 719 – 725.

Chapter 5

Structural stability and sound velocity of Kilauea basalt glass

The seismic velocities of natural Kilauea basalt glass are measured for multiple compression and decompression cycles up to 22 GPa at room temperature. The ambient shear and compressional velocities, 3.53(3) and 6.25(3) km/s respectively, exhibit pressure-induced softening to ~ 4 GPa, above which the velocities increases with pressure. On decompression, no hysteresis is seen to 14 GPa, indicating reversible compression and densification in this pressure range. However, below 14 GPa we observe significant hysteresis. When decompressed to nearly room pressure, the compressional velocity returns to the value measured before compression, suggesting that structural changes between 0 and 22 GPa are ultimately reversible.

The structure and physical properties of melts are important for understanding the dynamics of planetary interiors. The ascent of silicate melts in Earth's crust and mantle, stratification of igneous bodies, and planetary differentiation processes are all affected by the density contrast between melt and surrounding solid rock [*Schilling et al.,* 2003]. Density and compressibility are important for understanding melt segregation, yet the pressure and temperature derivatives of the elastic properties of melts with basaltic composition, for instance, are poorly known [*Kono et al.,* 2008]. One way to characterize silicate melt is to measure the physical and chemical properties of its quenched glass, because glass is simply the kinetically hindered form of the melt. In particular, any glass properties that do not show kinetic hindrances – with no indication of hysteresis, for example – can be considered to reflect melt properties, albeit at uncharacteristically low temperatures. Moreover, that the atomic-packing structure of glass is similar to that of the chemically comparable melt, so it is useful to document how pressure affects this structure as an indication of how melts evolve with depth (i.e., increased pressure) inside Earth.

High pressure Brillouin spectroscopy is an important tool for determining the acoustic velocities and elastic moduli of solids, including amorphous materials [*Dil,* 1982]. Here we present Brillouin scattering data of natural Kilauea basalt glass under several runs of quasi-hydrostatic compression and decompression to a maximum pressure of 22 GPa.

A parallel-faced fragment of natural basalt glass from Kilauea, HI (composition: SiO_2: 49.67, TiO_2: 2.91, Al_2O_3: 13.49, FeO: 14.24, MnO: 0.18, MgO: 5.94, CaO: 9.72, Na_2O: 2.56, K_2O: 0.69, grain formula weight: 63.596 [*Nelson and Carmichael*, 1979]) was polished on both sides to 30 μm thickness, and sliced into a 70 x 85 μm rectangle. Diamond-anvils (culet diameter of 300 μm) were used in a short symmetric cell with a rhenium gasket – initially 130 μm thick, pre-indented to 50 μm – and a 120 μm diameter hole contained the polished glass wafer, 3 ruby spheres as pressure calibrants [*Mao et al.,* 1978] and 4:1 methanol:ethanol mixture as the pressure transmitting medium. For a given pressure, we collected Brillouin spectra at 2 -3 locations across the sample with a collection time of 20 minutes per location.

Using confocal optics and 0.25-0.5 W of polarized $\lambda = 532$ nm radiation from a continuous-wave Nd:YVO_4 laser, spectra are obtained with a six-pass tandem (Sandercock) Fabry-Perot interferometer in either backscatter ($\theta = 180^\circ$) or equal-angle ($\theta = 70^\circ$) scattering geometry through a diamond-anvil cell. Measurements at two scattering angles (θ) allow us to determine the index of refraction (n) as well as the acoustic-wave velocities as a function of pressure from the sample inside the diamond-anvil cell [e.g., *Chen et al.,* 2010]. The 20 μm diameter laser beam at the sample and a fluorescence spectrometer integrated into the Brillouin system provide *in situ* pressure measurements without moving the sample. Our data collection sequence consisted of 3 consecutive runs (each run is a cycle of compression and decompression): Run 1, 0 – 22 – 0.5 (GPa); Run 2, 0.5 – 6.6 – 0.5 (GPa); Run 3, 0.5 – 7.2 – 0 (GPa). Equal-angle scattering data were collected in all three runs, whereas backscattering measurements were made only in run 1. Each spectrum is folded about the central Rayleigh peak to enhance the Brillouin signal from the sample [*Gleason et al.,* 2009]; peaks are fit with a Gaussian profile.

Equal-angle transmission through a parallel-sided sample, gives the wave velocity for shear (V_s) or compressional (V_p) modes via $V_{s,p} = \omega\lambda_0 \big/ 2\sin\left(\theta/2\right)$, where ω and λ_0 are the measured frequency shift and incident laser wavelength, respectively. The first compression-decompression cycle, 'Run 1' (circles, Figure 5.1) shows a velocity decrease up to 4.2 GPa for both shear and compressional modes. Then, with further compression (solid circles) velocity increases up to a maximum pressure of 22 GPa. On decompression (open circles), we see no evidence of hysteresis until ~14 GPa. Below 14 GPa, the V_p trend remains at a much higher velocity and returns to nearly 6.25(3) km/s at ambient conditions. Below ~10 GPa, the decompression V_s data of Run 1 are obscured by superposition of the compressional mode of methanol:ethanol. The next cycle, Run 2, (solid squares) again shows a velocity decrease with increasing pressure to ~5 GPa, and then increases to 7 GPa. On decompression (open squares), we see no hysteresis for either mode (i.e., mode softening is matched on decompression). For Run 3 (triangles), the V_p compression trend shows mode softening to 2.5 GPa and then an increase in the velocity with increasing pressure for V_p. The V_s trend for Run 3 is nearly linear from 3 – 7 GPa. On decompression, the V_s and V_p trends show no hysteresis.

Mode softening is seen in all runs for V_p on compression up to 5 GPa, and in V_s for Runs 1 and 2; this is corroborated by previous studies [*Zaug et al.,* 1992, their Fig. 14.; *Meng et al.,* 1987; *Schroeder et al.*, 1990]. For Run 1, we can distinguish two regions: 0 – 14 where there is significant hysteresis, and 14 – 22 GPa where there is no hysteresis.

These results suggest that at roughly 14 GPa there could be a structural transition, such as a change in first or more-distant neighbor coordination in the glass. For Runs 2 and 3, which remain below 14 GPa, V_p data show no hysteresis with decompression implying that whatever transition may take place must be above 7 GPa (maximum pressure achieved in Run 3). Also, all of our runs show V_p of the quenched sample being indistinguishable from that of the initial sample, indicating an ultimately reversible phenomenon. This is in contrast to soda-lime glass compressed to 14 GPa [*Tkachev et al.* 2005, their Fig. 1], which exhibits zero-pressure values well below the initial velocity after 3 decompression cycles, indicating some irreversible densification.

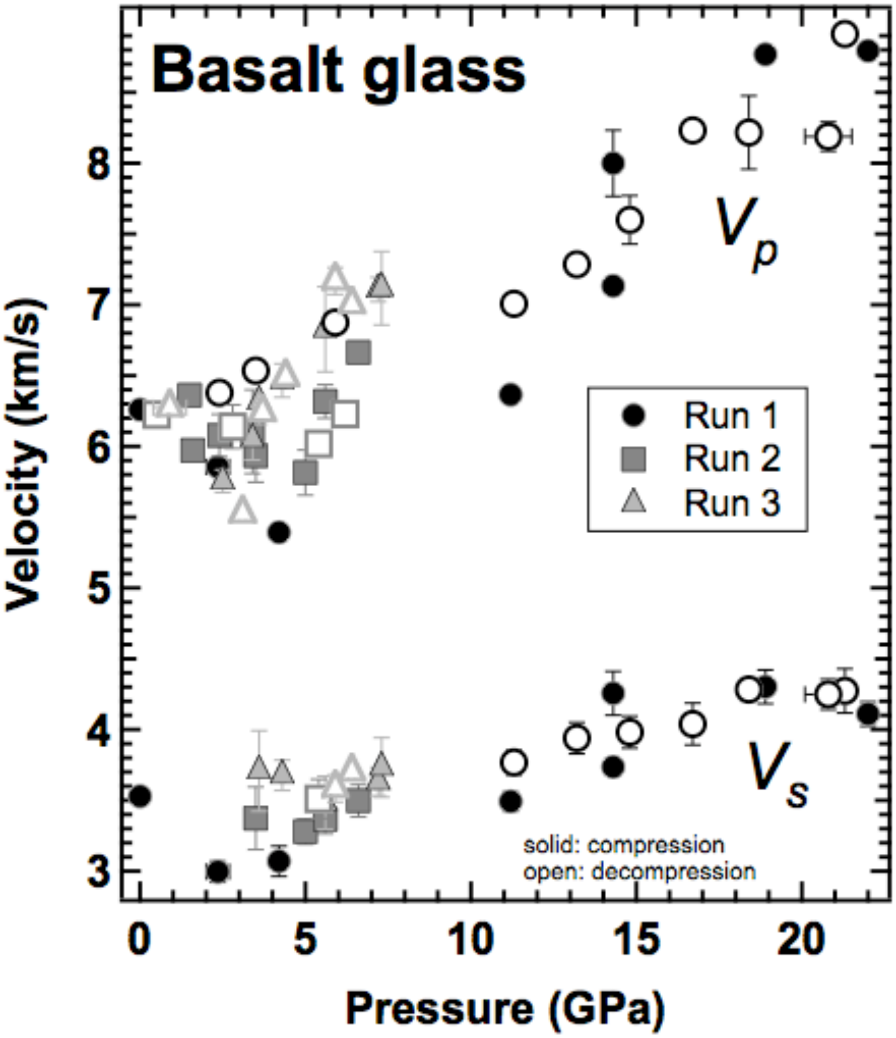

Figure 5.1: Compressional (V_P) and shear-wave (V_S) velocity measurements from equal-angle scattering geometry. Solid and open symbols are for compression and decompression, respectively. All results shown here are at room temperature.

Collecting spectra in two geometries, we determine shear- and compressional-wave velocities as well as n as a function of pressure [*Shimizu et al.,* 1998; *Sasaki et al.,* 2009], obtaining the refractive index from $n(P) = (\omega_{180}(P)/\omega_{70}(P))\sin(35°)$. We find that it increases smoothly from n = 1.58 to 1.77 (± 0.40) by 22 GPa (Figure 5.2). We find agreement between our refractive index trend and *Kuryaeva and Kirkinskii*'s [1997] data on basalt glass using interference-polarization microscopy.

The average isotropic elastic moduli are calculated from the measured compressional (V_p) and shear (V_s) wave velocities by $K_s = \rho\left(V_p^2 - 4V_s^2/3\right)$ and $G = \rho V_s^2$, where ρ, K_s and G are the density, adiabatic bulk and shear modulus, respectively (Figure 5.3). For Runs 1 and 2 the shear and bulk moduli decrease with increasing pressure up to ~5 GPa, and then increase with further compression. Similar behavior is documented for the bulk modulus of tholeiitic basalt and silica glass [*Kuryaeva and Kirkinskii*, 1997; *Kondo et al.*, 1981]. However, linearly fitting each data set gives K_{0s} = 63 (± 1) GPa, K_{0s}' = 4.6 (± 0.6), G_0 = 34.7 (± 0.5) GPa, and G_0‘ = 1.2 (± 0.2) (subscript zero and prime indicate zero-pressure conditions and pressure derivative, respectively). Our results are in close agreement with x-ray absorption/microtomography data on a USGS standard BCR-2 (Columbia River Basalt), which yielded K_0 = 70 (± 5) GPa [*Clark et al.,* 2009]. To compare these results with isothermally collected data, we employ $K_s = (C_p/C_v)K_T = \rho(C_p/C_v)(dP/d\rho)$, where C_p/C_v is the ratio of isobaric to isochoric specific heat. Experimental data on pressure dependent specific heats, thermal expansivity or Gruneisen parameter are not available for basalt glass, so we approximate C_p/C_v from amorphous silica [*Horbach et al.,* 1999] that gives a value ~1. We integrate $d\rho / dP = (C_p / C_v)/(V_p^2 - 4V_s^2/3)$ to determine the density as a function of pressure (Figure 5.3, inset, black curve).

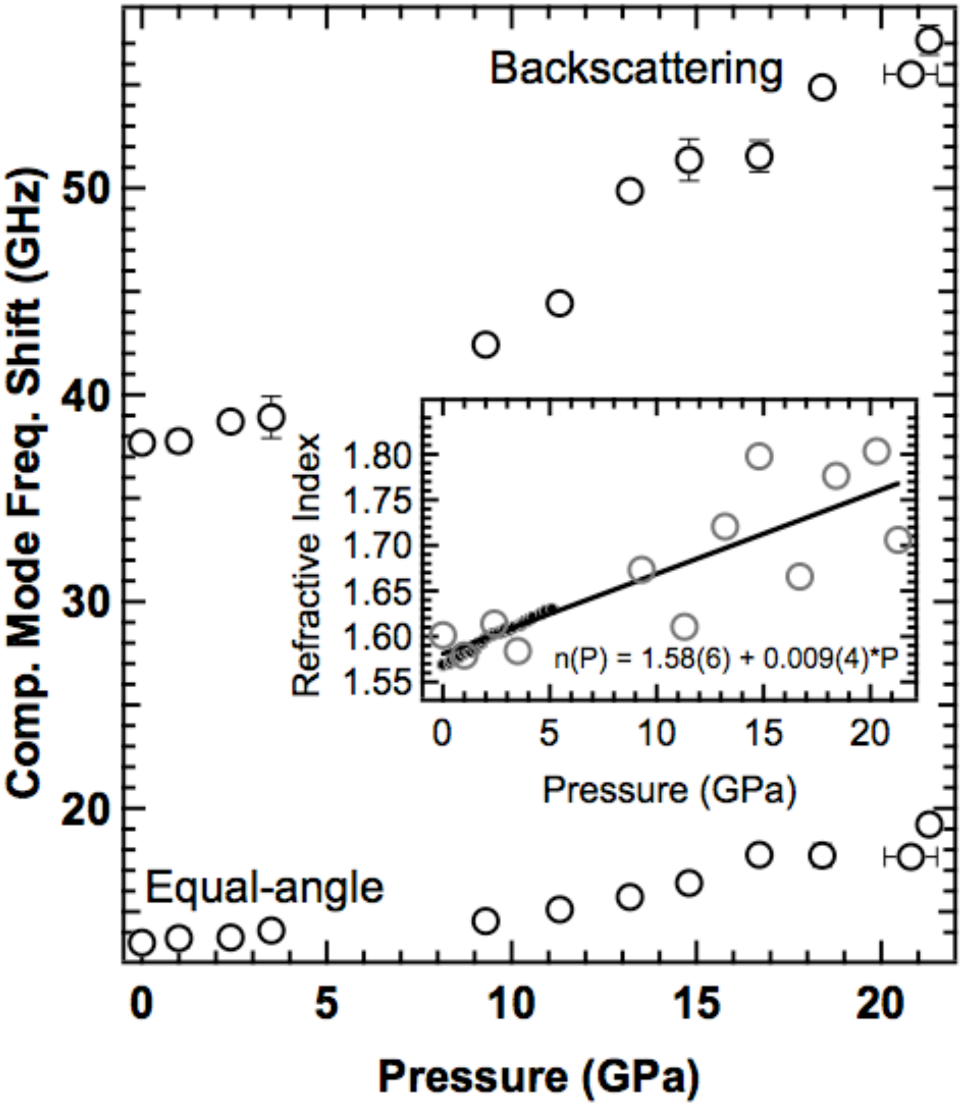

Figure 5.2: Compressional-mode Brillouin data for two scattering geometries, backscattering (θ = 180°) and equal-angle (θ = 70°), decompression only (open circles). *Inset:* Index of refraction determined as a function of pressure from the two sets of measurements (grey circles; black

curve is the best linear fit); small black circles are refractive index measurements from *Kuryaeva and Kirkinskii,* [1997].

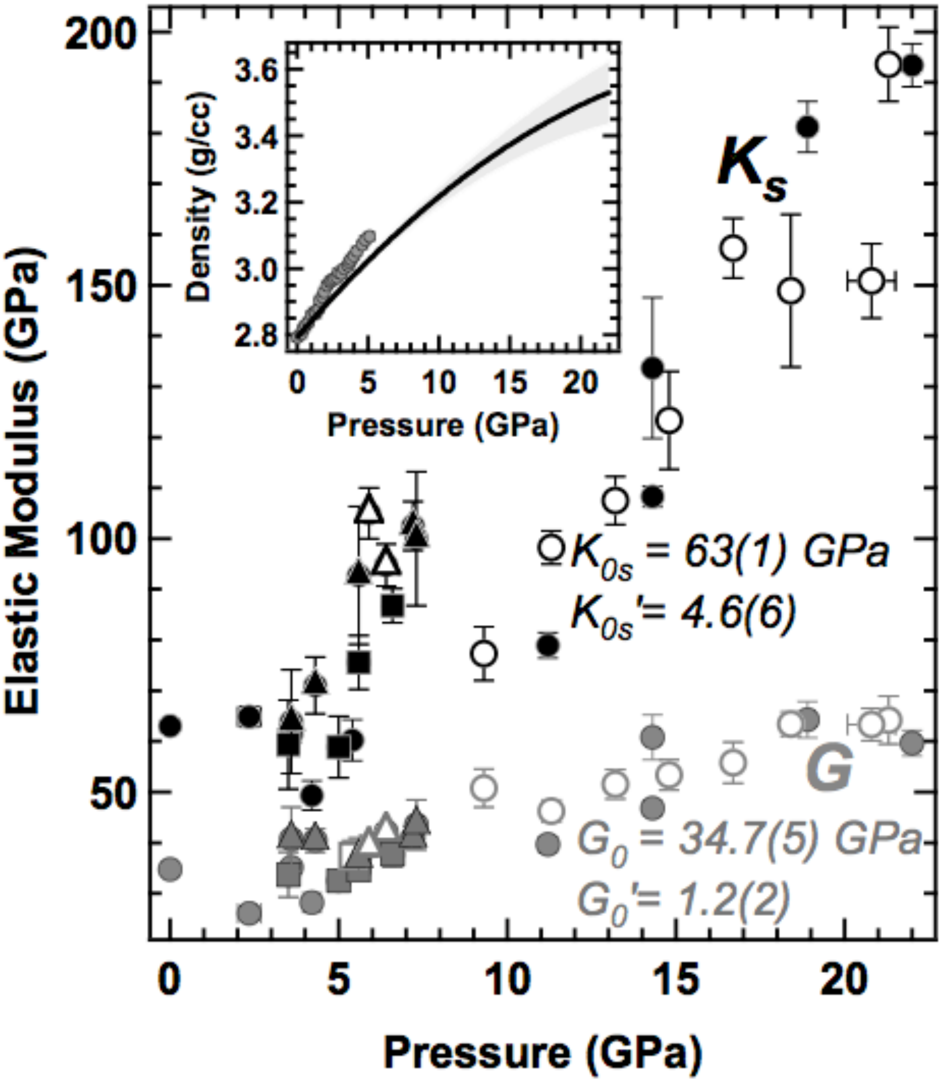

Figure 5.3: Shear (all grey data) and bulk (all black data) moduli with pressure derived from the Brillouin measurements. Linear fits yield K_{0s}, K_{0s}', G_0 and G_0'. Symbol scheme matches Figure 5.1. *Inset:* Density as a function of pressure obtained from integrating the Brillouin velocity measurements (thick solid black line, grey shaded area is uncertainty envelope) is compared to *Kuryaeva and Kirkinshii* [1997] (grey circles).

That the compressional velocity V_p returns to the pre-compressed value after 3 cycles implies a reversible change in the atomic-packing structure of the glass. Spectroscopic evidence for continuous and reversible coordination changes in amorphous silicate glasses has also been documented [*Williams and Jeanloz,* 1988, their Fig. 1]. As the glass state is the kinetically frozen state of the liquid, a reversible transformation occurring in the glass is expected also to occur in the corresponding liquid. Hence, the reversibility we observe in the Kilauea basalt glass' structural changes implies similar changes in the compositionally equivalent magma at high pressure.

The average Si-O-Si angle between silicon tetrahedra decreases on compression below 10 GPa, leading to a decrease in the size of the rings of tetrahedra making up the structure [*Peral and Iniguez,* 2006]. Above 20 GPa, the four-fold silicon coordination increases toward six-fold with some distortion [*Bernal*, 1959; *Finger and Hazen*, 1991]. If, with increasing pressure the structure of the liquid becomes more dense than the coexisting solid (due to higher coordination as well as differences in composition between crystals and melt), then the density of the liquid could exceed that of the solid silicates at high pressure, resulting in melt layers sinking at depth in Earth's mantle (e.g., 12 – 25 GPa) [*Williams and Jeanloz,* 1988]. This may be a key driving force for geochemical differentiation of terrestrial planets.

Bibliography

Bernal, J. (1959), A geometrical approach to the structure of liquids, *Nature, 183,* 141 – 147.

Chen, B., et al. (2010), Elasticity, strength, and refractive index of argon at high pressure, *Phys. Rev. B, 81*, 144110, doi: 10.1103/PhysRevB.81.144110.

Clark, A., et al. (2009), Density of BCR-2 basalt glass at high pressure by X-ray absorption microtomography, *AGU abs. #MR13A-1669.*

Dil, J. (1982), Brillouin scattering in condensed matter, *Rep. Prog. Phys., 45*, 285 – 334.

Finger, L. and R. Hazen (1991), Crystal chemistry of six-coordinated silicon: a key to understanding the Earth's deep interior, *Acta. Cryst., B47,* 561 – 580.

Gleason, A.E., et al. (2009), Grain-boundary effects in Brillouin scattering at ambient and high pressure, *Geophys. Res. Lett., 36*, L23309, doi:10.1029/2009GL040420.

Horbach, J., et al. (1999), Specific heat of amorphous silica within the harmonic approximation, *J. Phys. Chem. B, 103,* 4104 – 4108.

Kondo, K., et al. (1981), Non-linear pressure dependence of the elastic moduli of fused quartz up to 3 GPa, *J. Appl. Phys., 52,* 2826 – 2831.

Kono, Y., et al. (2008), Elastic wave velocities and Raman shift of MORB glass at high pressure, *J. Min. Pet. Sci*., *103*, 126 – 130.

Kuryaeva, R. and V. Kirkinskii (1997), Influence of high pressure on the refractive index and density of tholeiite basalt glass, *Phys. Chem. Min., 25,*48 – 54.

Mao, H.K., et al. (1978), Specific volume measurements of Cu, Mo, Pd, and Ag and calibration of the ruby R1 fluorescence pressure gauge from 0.06 to 1 Mbar, *J. Appl. Phys., 49*(6), 3276 – 3283, doi:10.1063/1.325277.

Meng, Y., et al. (1987), Investigation of the elastic behavior of SiO2 – TiO2 glasses under high pressure using Brillouin scattering, *EOS Trans. AGU, 68,* 1470.

Nelson, S. and I. Carmichael (1979), Partial molar volumes of oxide components in silicate liquids, *Contrib. Mineral. Petrol., 71,* 117 – 124.

Peral, I. and J. Iniguez (2006), Amorphization induced by pressure: Results for zeolites and general implications, *Phys. Rev. Lett. 97*, 225502.

Sasaki, S., et al., (2009), High-pressure Brillouin study of the elastic properties of rare-gas solid xenon at pressures up to 45 GPa, *J. Raman Spect., 40*(2)*,* 121 – 127.

Shimizu, H., et al. (1998), High-pressure elastic properties of liquid and solid krypton to 8 GPa, *Phys. Rev. B. 57,* 230 – 233.

Schilling, F., et al. (2003), Elastic properties of model basaltic melt compositions at high temperatures, *J. Geophys. Res., 108(B6),* 2304.

Schroeder, J., et al. (1990), Brillouin and Raman scattering from glasses under pressure, *High Press. Res., 4,* 531 – 533.

Tkachev, S. N., et al. (2005), In situ Brillouin spectroscopy of a pressure-induced apparent second-order transition in silicate glass, *Phys. Rev. Lett., 95*, 057402.

Williams, Q. and R. Jeanloz (1988), Spectroscopic evidence for pressure-induced coordination changes in silicate glasses and melts, *Science*, *239,* 902 – 905.

Zaug, J., et al. (1992), Elastic constants, equations of state and thermal diffusivity at high pressure, in *High-pressure research: application to earth and planetary science*, edited by M. Manghnani and Y. Syono, pp. 157 – 166, Terra Scientific Publishing Company, Tokyo.

Appendix A

Eulerian Equation of State Under Hydrostatic Stress

We aim to reproduced *Birch*'s [1978] Eqn. 10, retaining all of the elastic constants and pressure terms that originate from the same order in the free energy expansion. Using the Eulerian strain metric, *f*, we first determine all the constants (*a,b,c,d* and *e*) in the strain energy expansion. This will give pressure (*P*) as a function of *f*, K_0, K_0', K_0''. Differentiating this with respect to volume gives a general formula for *K*.

Expand strain energy in a taylor series to the 4th order:

$$\phi = a + bf + cf^2 + df^3 + ef^4 \qquad \text{(A.1)}$$

ϕ = Helmholtz's potential, and *f* as the negative of the Eulerian strain metric:

$$f = \frac{1}{2}\left[\left(\frac{V_0}{V}\right)^{2/3} - 1\right]. \qquad \text{(A.2)}$$

a,b,c,d and *e* are constants for which we solve.

From thermodynamics: $P = \left.\frac{-d\phi}{dV}\right|_T = \left.\frac{-d\phi}{dV}\right|_S$, where T, S are constant temperature or entropy, respectively. $P = \frac{-d\phi}{df}\frac{df}{dV}$

$$\frac{df}{dV} = \frac{-(1+2f)^{5/2}}{3V_0} \qquad \text{(A.3)}$$

$a = 0$, when f=0, ϕ =0. $-\frac{d\phi}{df} = -(b + 2cf + 3df^2 + 4ef^3)$

$b = 0$, when $P = 0$, $V = V_0, f = 0$.

$$P = \frac{2cf(1+2f)^{5/2}}{3V_0} + \frac{df^2(1+2f)^{5/2}}{V_0} + \frac{4ef^3(1+2f)^{5/2}}{3V_0} \qquad \text{(A.4)}$$

Definition of the bulk modulus: $K = \frac{-VdP}{dV} = -V\frac{dP}{df}\frac{df}{dV}$ (A.5)

$$\frac{dP}{df} = \frac{10cf}{3V_0}(1+2f)^{3/2} + \frac{2c}{3V_0}(1+2f)^{5/2} + \frac{5df^2}{V_0}(1+2f)^{3/2} + \frac{2df}{V_0}(1+2f)^{5/2}$$
$$+ \frac{20ef^3}{3V_0}(1+2f)^{3/2} + \frac{4ef^2}{V_0}(1+2f)^{5/2}$$

$$K = \frac{V}{3{V_0}^2}(1+2f)^4\left(\frac{10cf}{3} + \frac{2c}{3}(1+2f) + 5df^2 + 2df(1+2f) + \frac{20ef^3}{3} + 4ef^2(1+2f)\right) \tag{A.6}$$

$c = \dfrac{9K_0V_0}{2}$, when $K = K_0$, $V = V_0$, $f = 0$.

$$P = 3K_0f(1+2f)^{5/2} + \frac{df^2(1+2f)^{5/2}}{V_0} + \frac{4ef^3(1+2f)^{5/2}}{3V_0} \tag{A.7}$$

Put c into (A.6), and in terms of f only:

$$\begin{aligned} K = {} & K_0(1+2f)^{5/2} + 5fK_0(1+2f)^{5/2} + 2fK_0(1+2f)^{5/2} + \frac{3df^2}{V_0}(1+2f)^{5/2} \\ & + \frac{2df}{3V_0}(1+2f)^{5/2} + \frac{4ef^2}{3V_0}(1+2f)^{5/2} + \frac{20ef^3}{9V_0}(1+2f)^{5/2} + \frac{8ef^3}{3V_0}(1+2f)^{5/2} \end{aligned} \tag{A.8}$$

$$\begin{aligned} \frac{dK}{df} = {} & 5K_0(1+2f)^{3/2} + 35fK_0(1+2f)^{3/2} + 7K_0(1+2f)^{5/2} + \frac{15df^2}{V_0}(1+2f)^{3/2} \\ & + \frac{6df}{V_0}(1+2f)^{5/2} + \frac{10df}{3V_0}(1+2f)^{3/2} + \frac{2d}{3V_0}(1+2f)^{5/2} + \frac{20ef^2}{3V_0}(1+2f)^{3/2} + \frac{8ef}{3V_0}(1+2f)^{5/2} \\ & + \frac{100ef^3}{9V_0}(1+2f)^{3/2} + \frac{60ef^2}{9V_0}(1+2f)^{5/2} + \frac{40ef^3}{3V_0}(1+2f)^{3/2} \\ & + \frac{8ef^2}{V_0}(1+2f)^{5/2} \end{aligned} \tag{A.9}$$

$$\frac{df}{dV}\frac{dK}{df} = \frac{dK}{dV} = \left(\frac{-(1+2f)^4}{V_0}\right)\frac{12K_0}{3} + \frac{49fK_0}{3} + \frac{2df}{V_0} + \frac{9df^2}{V_0} + \frac{2d}{9V_0} + \frac{14df}{9V_0} + \frac{8ef}{9V_0} + \frac{60ef^2}{9V_0} + \frac{60ef^2}{27V_0} + \frac{484ef^3}{27V_0} \tag{A.10}$$

$d = \dfrac{9V_0K_0K_0'}{2} - 18V_0K_0$, when $K' = K'_0$, $K = K_0$, $f=0$.

$$P = 3K_0f(1+2f)^{5/2} + (9K_0K_0' - 36K_0)\frac{f^2(1+2f)^{5/2}}{2} + \frac{4ef^3(1+2f)^{5/2}}{3V_0} \tag{A.11}$$

To solve for e, use:

$$\begin{aligned} K'' & = \left(\frac{d}{df}\frac{dK}{df}\right)\left(\frac{df}{dP}\right)^2 + \left(\frac{d}{dP}\frac{df}{dP}\right)\frac{dK}{df} \\ & = \quad \mathrm{A} \qquad\quad \mathrm{B} \qquad + \qquad \mathrm{C} \qquad\quad \mathrm{D} \end{aligned} \tag{A.12}$$

$$\begin{aligned} \frac{dP}{df} = {} & 15K_0f(1+2f)^{5/2} + 3K_0(1+2f)^{5/2} + \frac{45K_0K_0'f^2(1+2f)^{3/2}}{2} + 9K_0K_0'f(1+2f)^{5/2} \\ & + \frac{-180K_0f^2(1+2f)^{3/2}}{2} + -36K_0f(1+2f)^{5/2} + \frac{20ef^3(1+2f)^{3/2}}{3V_0} + \frac{4ef^2(1+2f)^{5/2}}{V_0} \end{aligned} \tag{A.13}$$

$$\begin{aligned} [\mathrm{D}] = \frac{dK}{df} = {} & 5K_0(1+2f)^{3/2} + -25fK_0(1+2f)^{3/2} + -5K_0(1+2f)^{5/2} + \frac{135f^2K_0K_0'}{2}(1+2f)^{3/2} \\ & + -270f^2K_0(1+2f)^{3/2} + 27fK_0K_0'(1+2f)^{5/2} + -108fK_0(1+2f)^{5/2} + 15fK_0K_0'(1+2f)^{3/2} \\ & + 3K_0K_0'(1+2f)^{5/2} + \frac{20ef^2}{3V_0}(1+2f)^{3/2} + \frac{8ef}{3V_0}(1+2f)^{5/2} + \frac{100ef^3}{9V_0}(1+2f)^{3/2} \\ & + \frac{60ef^2}{9V_0}(1+2f)^{5/2} + \frac{40ef^3}{3V_0}(1+2f)^{3/2} + \frac{8ef^2}{V_0}(1+2f)^{5/2} \end{aligned} \tag{A.14}$$

$$
\begin{aligned}
[\mathrm{A}] = \frac{d}{df}\left(\frac{dK}{df}\right) &= 15K_0(1+2f)^{1/2} + -75fK_0(1+2f)^{1/2} + -50K_0(1+2f)^{3/2} + \frac{405f^2K_0K_0'}{2}(1+2f)^{1/2} + 270fK_0K_0'(1+2f)^{3/2} \\
&+ -810f^2K_0(1+2f)^{1/2} + -1080fK_0(1+2f)^{3/2} + 27K_0K_0'(1+2f)^{5/2} + -108K_0(1+2f)^{5/2} \\
&+ 45fK_0K_0'(1+2f)^{1/2} + 30K_0K_0'(1+2f)^{3/2} + \frac{20ef^2}{V_0}(1+2f)^{1/2} + \frac{80ef}{3V_0}(1+2f)^{3/2} + \frac{8e}{3V_0}(1+2f)^{5/2} \\
&+ \frac{220ef^3}{3V_0}(1+2f)^{1/2} + \frac{200ef^2}{3V_0}(1+2f)^{3/2} + \frac{264ef}{9V_0}(1+2f)^{5/2} + \frac{80ef^2}{V_0}(1+2f)^{3/2}\frac{3}{3}
\end{aligned}
$$

$$[\mathrm{B}] = \left(\frac{(1+2f)}{3K}\right)^2 \tag{A.15}$$

$$[\mathrm{C}] = \frac{2+4f+-3K'+-6fK'}{9K^2} \tag{A.16}$$

Evaluate (A.12) with *K'' = K₀''; K' = K₀'; K=K₀; f=0* to solve for e:

$$[\mathrm{A}]*[\mathrm{B}] = \frac{-143+57K_0{}'}{9K_0} + \frac{8e}{V_0K_0{}^2 27} \qquad [\mathrm{C}]*[\mathrm{D}] = \frac{2K_0'}{3K_0} + \frac{-(K_0'^2)}{K_0} \tag{A.17}$$

$$e = \frac{V_0K_0{}^2 27(9K_0''K_0 + 9K_0'^2 + 143 - 63K_0{}')}{(8)9K_0} \tag{A.18}$$

$$P = 3K_0f(1+2f)^{5/2} + (9K_0K_0' - 36K_0)\frac{f^2(1+2f)^{5/2}}{2} + \frac{f^3}{2}K_0(1+2f)^{5/2}(9K_0''K_0 + 9K_0'^2 + 143 - 63K_0{}') \tag{A.19}$$

Eqn. (A.19) matches Birch,[13] his Eqn 8.

Differentiate (A.19); multiply by *–V* and *df/dV* to get $K_{general}$:

$$
\begin{aligned}
\frac{dP}{df} &= 15K_0f(1+2f)^{3/2} + 3K_0(1+2f)^{5/2} + \frac{45f^2K_0K_0'}{2}(1+2f)^{3/2} + 9fK_0K_0'(1+2f)^{5/2} \\
&+ -90f^2K_0(1+2f)^{3/2} + -36fK_0(1+2f)^{5/2} + \frac{5}{2}f^3K_0{}^2K_0''(1+2f)^{3/2} + 27\frac{f^2}{2}K_0{}^2K_0''(1+2f)^{5/2} \\
&+ \frac{45f^3}{2}K_0K_0'^2(1+2f)^{3/2} + \frac{27f^2}{2}K_0K_0'^2(1+2f)^{5/2} + \frac{-315f^3}{2}K_0K_0{}'(1+2f)^{3/2} \\
&+ \frac{-189f^2}{2}K_0K_0{}'(1+2f)^{5/2} + 715\frac{f^3}{2}K_0(1+2f)^{3/2} + \frac{429f^2}{2}K_0(1+2f)^{5/2}
\end{aligned}
\tag{A.20}
$$

$$
\begin{aligned}
K = K_0(1+2f)^{5/2}[1 - 5f + 3fK_0' + \frac{35f^2}{2} + 18f^2K_0' + \frac{9f^2}{2}K_0K_0'' + \frac{9f^2}{2}K_0'^2 \\
+ \frac{1573f^3}{6} + \frac{59f^3K_0K_0''}{6} + \frac{33f^3K_0'^2}{2} + \frac{-231f^3K_0{}'}{2}]
\end{aligned}
\tag{A.21}
$$

The first seven terms inside the brackets of (A.21) are *exactly* what *Birch* [1978] lists in his Eqn. 10, and the following terms originate from the same order in the free energy expansion.

Bibliography

Birch, F. (1978), Finite strain isotherm and velocities for single-crystal and polycrystalline NaCl at high pressures and 300°K. *J. Geophys. Res., 83*, 1257 – 1268.